

OMNILENS++: BLIND LENS ABERRATION CORRECTION VIA LARGE LENSLIB PRE-TRAINING AND LATENT PSF REPRESENTATION

Qi Jiang^{1,*} Xiaolong Qian^{1,*} Yao Gao¹ Lei Sun^{2,†} Kailun Yang³ Zhonghua Yi¹

Wenyong Li¹ Ming-Hsuan Yang^{4,5} Luc Van Gool² Kaiwei Wang^{1,†}

¹Zhejiang University ²INSAIT, Sofia University “St. Kliment Ohridski”

³Hunan University ⁴University of California, Merced ⁵Google DeepMind

ABSTRACT

Emerging deep-learning-based lens library pre-training (LensLib-PT) pipeline offers a new avenue for blind lens aberration correction by training a universal neural network, demonstrating strong capability in handling diverse unknown optical degradations. This work proposes the OmniLens++ framework, which resolves two challenges that hinder the generalization ability of existing pipelines: the difficulty of scaling data and the absence of prior guidance characterizing optical degradation. To improve data scalability, we expand the design specifications to increase the degradation diversity of the lens source, and we sample a more uniform distribution by quantifying the spatial-variation patterns and severity of optical degradation. In terms of model design, to leverage the Point Spread Functions (PSFs), which intuitively describe optical degradation, as guidance in a blind paradigm, we propose the Latent PSF Representation (LPR). The VQVAE framework is introduced to learn latent features of LensLib’s PSFs, which is assisted by modeling the optical degradation process to constrain the learning of degradation priors. Experiments on diverse aberrations of real-world lenses and synthetic LensLib show that OmniLens++ exhibits state-of-the-art generalization capacity in blind aberration correction. Beyond performance, the AODLibpro is verified as a scalable foundation for more effective training across diverse aberrations, and LPR can further tap the potential of large-scale LensLib. The source code and datasets will be made publicly available at <https://github.com/zju-jiangqi/OmniLens2>.

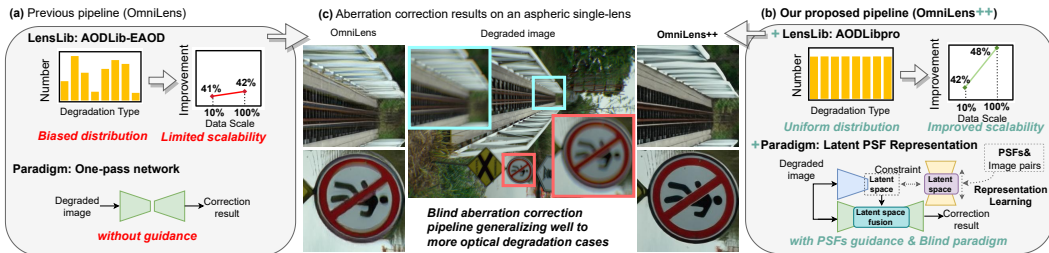


Figure 1: This work addresses the challenges of the current LensLib-PT pipeline. (a) OmniLens suffers from limited data scalability arising from the biased data distribution and lack of prior guidance for the model. (b) In OmniLens++, the proposed AODLibpro reveals uniform distribution contributing to improved scalability, while the latent PSF representation provides effective prior guidance with blind paradigm. (c) OmniLens++ effectively resolves the failure case of OmniLens.

*Equal contribution.

†Corresponding authors.

1 INTRODUCTION

Lens aberrations, typically arising from compromised image quality optimization due to design trade-offs for specific requirements, *e.g.*, minimalist optical systems (Heide et al., 2013; Peng et al., 2019), or lenses on mobile devices (Chen et al., 2023), and manufacturing/assembly errors (Liu et al., 2024) in complex systems, introduce blur to the captured images. This blur is also referred to as optical degradation (Chen et al., 2021b), characterized by its distinctive spatially-varying nature where degradation varies across Field-of-Views (FoVs) and exhibits diverse patterns depending on optical path, representing a fundamental image quality issue but has received limited attention in the learning and vision literature. With the advancement of image processing, computational post-processing (Schuler et al., 2011) has become a mainstream pipeline, also known as computational aberration correction. Unlike non-blind methods that rely on precise Point Spread Functions (PSFs) calibration (Chen et al., 2025), the blind pipeline (Schuler et al., 2012) offers more flexible and user-friendly advantages for users without optical expertise, where only the captured images are required for high-quality results. Recently, the deep learning-based Lens Library Pre-Training pipeline (LensLib-PT) has emerged as a powerful blind aberration correction paradigm (Gong et al., 2024). A universal network is trained to learn the mapping from diverse aberration distributions to clear images, demonstrating advantages over traditional blind deconvolution methods (Eboli et al., 2022) in terms of generalization to different optical degradation types. In particular, the OmniLens framework (Jiang et al., 2024b) delivers strong performance, enabled by a large-scale LensLib consisting of automatically designed lens samples to cover diverse real-world aberration distributions.

Building upon this paradigm, as shown in Figure 1, this paper further proposes *OmniLens++* as a robust solution to blind lens aberration correction, with particular focus on addressing two key challenges in OmniLens: 1) the *scalability* of LensLib is limited; 2) the aberration correction model lacks *guidance* to adaptively process diverse aberration distributions.

The OmniLens framework has laid the groundwork for high-quality LensLib construction by leveraging the Evolution-based Automatic Optical Design (EAOD) method (Jiang et al., 2024b) to generate large-scale lens sources. However, as shown at the top of Figure 1 (a), the constructed AODLib-EAOD reveals biased optical degradation distribution. This stems from several missing specifications in its lens-source generation process, and from which the applied sampling basis based on lens design indicators (average RMS spot radius) can hardly characterize the severity and spatial variation patterns of aberrations (Zhou et al., 2024). Consequently, the scalability of such a LensLib remains limited, where increasing the data scale fails to compensate for the absence of certain degradation types. To this end, we put forward a novel hybrid sampling basis to encompass any possible optical degradation patterns, which quantify the severity and spatial variation trends of optical degradation from the per-FoV image quality of lens imaging results rather than lens design indicators. As depicted at the top of Figure 1 (b), supplemented with enriched design specifications, the hybrid sampling contributes to the *large LensLib AODLibpro* with uniform aberration distributions without bias. The trained universal model can benefit from its scalability and achieve significant improvements with large-scale data. In addition, a synthetic benchmark is also established on the sampled lenses for evaluating aberration correction methods in terms of model design, which is also the first benchmark in this field for comprehensive evaluation across diverse aberration patterns.

Beyond constructing scalable data resources, an equally important challenge lies in designing models that can effectively handle diverse degradation types. Introducing degradation prior representation as guidance is a crucial design for such universal models (Potlapalli et al., 2023; Hu et al., 2025). In aberration correction, PSFs serve as an intuitive representation of degradation. Whether through explicit deconvolution (Lin et al., 2022) or implicit representation embedding (Jiang et al., 2024a), correction results can be effectively improved. However, these approaches require precise PSFs of the used lenses, which is infeasible in a blind pipeline. To this end, we propose the *Latent PSF Representation (LPR)* method, which predicts PSF information from degraded images in latent space, enabling a *blind paradigm while ensuring effective guidance of degradation priors* (at the bottom of Figure 1 (b)). LPR is motivated by encoding the optical priors embedded in PSFs, enabling their direct retrieval from degraded images to guide aberration correction. During representation learning, key PSF features modeling the optical degradation priors are learned and stored via self-supervised PSF reconstruction based on VQVAE (van den Oord et al., 2017) under the regularization of the forward operator of optical degradation. The Foundational Computational Aberration Correc-

tion (FoundCAC) model is then proposed, containing an independent encoder to extract degradation priors from images under the constraint of the learned LPR for latent space feature fusion.

Extensive experiments across diverse types of minimalist optical systems, misaligned lenses, high-end lenses, and our benchmark demonstrate that OmniLens++ achieves state-of-the-art performance in blind aberration correction. Taking an aspheric single-lens as an example, Figure 1 (c) illustrates that OmniLens++ can handle the failure case of OmniLens (Jiang et al., 2024b). Furthermore, we verify that: 1) scaling AODLibpro yields considerable improvements; 2) LPR-based guidance is more effective than other competing representation methods; and 3) LPR facilitates the model to sufficiently exploit the potential of large-scale AODLibpro.

The main contributions of this work are:

- We introduce OmniLens++, a LensLib-PT-based framework for blind aberration correction that achieves zero-shot generalization across diverse real-world lenses.
- We put forward AODLibpro, which enables a scalable data source by enriching the lens source coverage and sampling uniform-distributed optical degradation patterns.
- We propose the Latent PSF Representation (LPR) that enables the blind paradigm while injecting PSF-derived degradation priors to guide aberration correction.

2 RELATED WORK

Lens aberration correction through post-processing is widely applied in computational imaging, commonly used for Minimalist Optical System (MOS) imaging (Wei et al., 2024; Qian et al., 2025; Tseng et al., 2021) and image quality enhancement for mobile devices (Chen et al., 2023; Schuler et al., 2012). The non-blind methods with one-lens-one-solution paradigm (Chen et al., 2021b; Yanny et al., 2022) represent the current mainstream research direction. However, the required processes of complex calibration (Chen et al., 2025) and model training (Chen et al., 2021a) for each different lens make it unfriendly to users without optical backgrounds. Blind pipelines offer a more flexible solution, requiring only degraded images as input. Traditional methods typically revolve around kernel estimation, using estimated kernels for non-blind deconvolution, compensated by natural image priors (Kee et al., 2011; Schuler et al., 2012; Yue et al., 2015; Eboli et al., 2022), but limited to handling mild aberrations, which can hardly generalize to more diverse lens types. The recent data-driven Lens Library Pre-Training (LensLib-PT) pipeline addresses this issue by training a universal correction model on a LensLib covering diverse aberration distributions. Early work (Li et al., 2021; Gong et al., 2024) leverages few manually collected lens samples, where the scalability constraints result in limited coverage. While Zernike-based virtual databases (Hu et al., 2021; Jiang et al., 2024c) contribute to data expansion, they suffer from shortcomings in the realism of distributions. In comparison, AODLib-EAOD constructed by EAOD algorithms in OmniLens achieves a balance between data scale and aberration distribution authenticity (Jiang et al., 2024b). Nevertheless, expanding the scale of AODLib-EAOD yields limited improvements, which is due to the lack of specifications in lens sources, and the data bias introduced by a simple sampling basis. To this end, this work incorporates more design specifications into AOD for broader coverage. A hybrid sampling basis is then designed based on the quantification of both severity and spatial-varying trends of optical degradation to eliminate the data bias.

Representation of degradation priors is widely studied in All-in-One Image Restoration (AIO-IR) to guide models in processing different degradation types (Jiang et al., 2025a), yet remains under-explored in lens aberration correction. AIO-IR methods typically employ visual prompts (Potlapalli et al., 2023; Ma et al., 2023), contrastive learning (Li et al., 2022), text semantic prompts Ai et al. (2024), large model based feature extraction (Zhang et al., 2025), and pretext tasks (Hu et al., 2025) to characterize categorical information of different degradations. Unlike AIO-IR, where degradations differ in underlying causes, different degradations in lens aberration correction all stem from convolution-induced image blur, varying primarily in severity and spatial-varying patterns, making category-based designs inapplicable. Given that PSFs directly characterize such degradations, several works propose using PSF information to guide aberration correction, achieving remarkable improvements via intuitive deconvolution design (Li et al., 2021; Lin et al., 2022) or PSF-guided deep feature fusion (Jiang et al., 2024a; Luo et al., 2024). However, requiring precise PSFs for each lens during inference prevents these efforts from operating under blind paradigms. To leverage PSF-based guidance while achieving blind operation, this work explores predicting PSF-related in-

formation from degraded images to guide the aberration correction process. VQVAE (van den Oord et al., 2017) provides insights by utilizing VQ codebooks (Esser et al., 2021) in latent space to store key features, which has been investigated to represent optical degradation priors for guiding aberration correction Chen et al. (2023); Jiang et al. (2025b). Inspired by this, we propose LPR, which applies reconstruction to PSFs for storing key features, and contains a forward operator of optical degradation to constrain the codebook to learn latent PSF features describing optical priors.

3 METHODOLOGY

3.1 MOTIVATION

Building a Lenslib-PT-based blind aberration correction framework hinges on two axes: 1) the coverage and aberration distribution of Lenslib decides the application scope of the trained model; and 2) the model paradigm determines whether it can leverage the potential of the data. Therefore, we consider both aspects to train a foundational model with stronger generalization ability.

LensLib construction. Figure 1 (c) shows that the lack of the aspheric surface in specifications makes OmniLens (Jiang et al., 2024b) fail on such lenses, indicating that missing specifications lead to insufficient coverage of certain OD distributions in the lens source. *More specifications should be included to increase the diversity of aberrations coverage during the lens source generation stage.* Meanwhile, Figure 1 (a) shows that expanding the scale of AODLib-EAOD from 10% to 100% yields limited improvements, highlighting the challenge of enlarging the data scale. This is mainly due to its RMS-based sampling basis, since RMS cannot describe the spatial-varying patterns of optical degradation, or even reflect its severity (Zhou et al., 2024). This leads to the fact that increasing the data scale fails to compensate for the absence of certain degradation types. *Designing a hybrid sampling basis that jointly considers spatial-varying properties and severity of optical degradation* comes to the forefront.

Model paradigm. Table 1 shows the performance of several existing aberration correction model paradigms, among which using Ground-Truth (GT) PSFs to guide the model demonstrates great potential. However, for the blind paradigm, its required PSF information is unavailable. Directly predicting PSFs from degraded images (the third row of Table 1) is an intuitive pipeline, but such a task is revealed to be an ill-posed problem (Joshi et al., 2008; Rego et al., 2021), which can hardly reach the performance of GT-PSFs-guided pipeline. To this end, we attempt to predict PSF features in the latent space as guidance (the fourth row of Table 1). This strategy alleviates the prediction difficulty to some extent, but remains constrained by the large discrepancy between degraded images and PSFs. To further promote convincing PSF information prediction in latent space, *we aim to design an effective representation that retains informative PSF features* by leveraging the vector quantization and feature matching strategy in VQVAE (van den Oord et al., 2017).

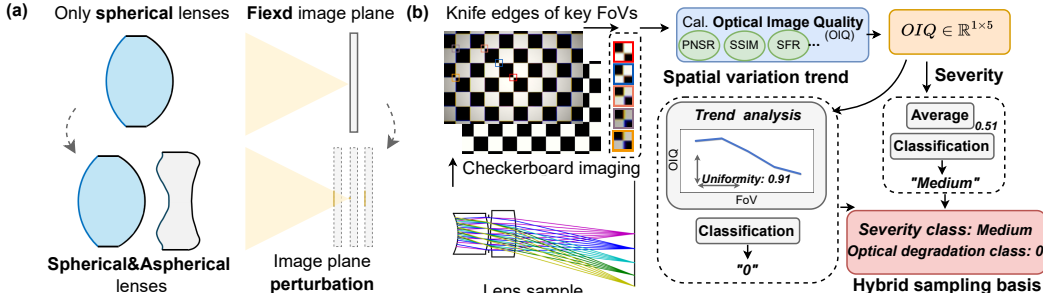


Table 1: Results of existing model paradigms on the benchmark set up in Section 3.2. Settings are detailed in Appendix C.

Paradigm	Blind	PSNR	SSIM	LPIPS
Baseline	✓	26.10	0.837	0.1701
GT-PSFs-guided	✗	28.73	0.873	0.1269
PSFs prediction	✓	28.25	0.861	0.1283
PSFs feature prediction	✓	28.42	0.867	0.1287

Figure 2: Illustration of the key designs in constructing AODLibpro. We expand surface type and imaging distance specifications in (a) to realize a broader set of optical degradation patterns during lens source generation; and quantify degradation severity and spatial variation trends via image quality assessment in (b), yielding a hybrid sampling that covers plausible optical degradation patterns.

3.2 DATA PREPARATION STAGE: LARGE LENSLIB CONSTRUCTION

Generation of lens source. To preserve diversity and realism in LensLib, we retain EAOD (Jiang et al., 2024b) for generating the lens source based on different sets of design specifications. We refer readers to (Jiang et al., 2024b) for details on EAOD. Building on this, we incorporate two influential yet previously omitted specifications to further diversify the lens source as shown in Figure 2 (a): (i) aspheric surface to broaden reachable degradation patterns, where high-order aspheric coefficients are added to lens parameters and EAOD’s ray tracing is modified to handle aspheric surface case following (Chen et al., 2021b); and (ii) image distance, which shifts the focal field and shapes spatial degradation characteristics. To model the latter, we perturb the image distance of EAOD-optimized lenses with probability γ within their depth of field to yield an additional variant sample. Finally, we feed all specifications into EAOD to search for candidate solutions to constitute the lens source. More details on the two specifications can be found in Appendix D.

Hybrid sampling basis. Since traditional design indicators do not fully capture the optical degradation of a lens in the image domain (§ 3.1), we quantify optical degradation by assessing the image quality of a lens’s imaging results. We quantify per-FoV severity and categorize optical degradation by its variation trend to enable balanced sampling covering possible degradation patterns. Concretely, as in Figure 2 (b), a degraded checkerboard of the target lens and its paired GT are applied as the quantification base. Five knife-edge image patches sampled from the center to periphery FoVs are cropped for quantification. The Optical Image Quality (OIQ) is assessed to grade per-FoV degradation severity, where we adopt the weighted sum of fidelity metrics (PSNR and SSIM) and optical metric (SFR) as a prototype of OIQ. The average OIQ across the 5 FoVs is applied as the overall degradation severity of the target lens. For the entire lens source, we analyze the per-sample average OIQ distribution and partition the severity into 3 classes as *Strong*, *Medium*, and *Mild*. Furthermore, we categorize spatial variation patterns of optical degradation by defining 6 Optical Degradation Class (OD-Class) from OIQ trends over FoVs. First, using the variance and mean of per-FoV OIQ, we compute the coefficient of variation to measure spatial uniformity U_S . Samples with values above a threshold α are labeled the “*spatial-uniform*” OD-Class. For $U_S < \alpha$, 5 *additional* OD-Class are defined by the *FoV of peak OIQ* and the *monotonicity of OIQ changes*. In this way, average OIQ and OD-Class serve as the hybrid sampling basis for sampling a uniform OD distribution. Detailed OIQ computation and OD-Class definitions are provided in Appendix D.

Construction of AODLibpro. With the novel sampling basis, we propose AODLibpro by sampling a balanced set from the lens source with uniform coverage over severity and spatial-variation patterns. We form 18 OD sub-classes by crossing the average OIQ category with OD-Class. From each subclass, m_1 and m_2 instances are sampled to build AODLibpro `train` and `test`, respectively. The former offers large-scale training supervision, and the latter serves as a comprehensive benchmark to evaluate the performance of the potential networks across diverse aberration distributions.

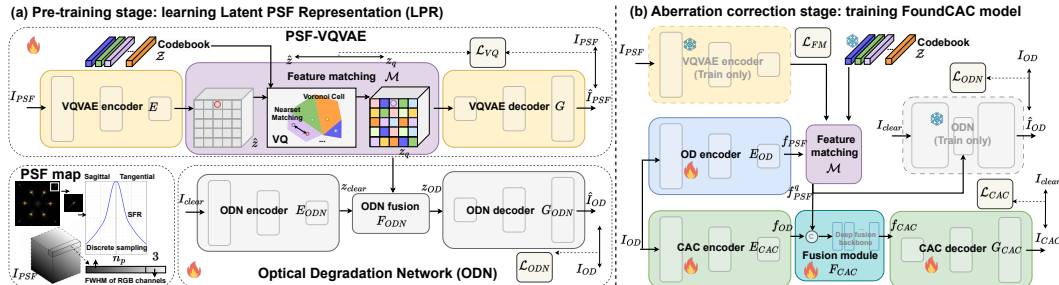


Figure 3: Overview of the proposed FoundCAC model guided by pre-trained LPR. (a) Pre-training stage for learning LPR. PSF-VQVAE explicitly stores the key latent PSF features regularized by ODN for modeling optical priors. (b) Aberration correction stage for training FoundCAC. The latent PSF features are predicted for guiding the correction model, regularized by the learned LPR.

3.3 STAGE I: LEARNING LATENT PSF REPRESENTATION

As shown in Figure 3 (a), we pretrain a Latent PSF Representation (LPR) to encode rich optical priors from PSFs, where a VQVAE codebook materializes key features, and an Optical Degradation Network (ODN) supervises and regularizes optical priors learning, supporting effective latent PSF feature prediction during the aberration correction stage.

PSF-VQVAE. To represent PSFs as an information modality that is pixel-aligned with the degraded image $I_{OD} \in \mathbb{R}^{H \times W \times 3}$, PSF kernels are converted into a PSF map $I_{PSF} \in \mathbb{R}^{H \times W \times N_p}$. For each pixel, we compress the PSF at its corresponding FoV and reshape it into a feature vector $x_p \in \mathbb{R}^{1 \times 1 \times N_p}$ along the channel dimension for insertion. To improve the information density of the compressed PSFs, following (Chen et al., 2023), we compute the SFR for PSFs supplemented with the PSFs' per-channel full width at half maximum (FWHM) to serve as x_p . The dimensionality of x_p is $N_p = n_p + 3$, where n_p is the resolution of the discrete sampling of the SFR curve. Then, the key lies in learning optical priors from the PSF map. VQVAE (van den Oord et al., 2017) learns a discrete latent prior into a codebook, providing transferable representations that can be directly retrieved. Motivated by this property, we propose PSF-VQVAE as the basis for LPR. The PSF map I_{PSF} is mapped into the latent feature $\hat{z} \in \mathbb{R}^{H/8 \times W/8 \times n_z}$ with spatial size $(H/8 \times W/8)$ and channel dimension n_z by the VQVAE encoder E , which is quantized by the codebook $\mathcal{Z} = \{z_k\}_{k=1}^K \in \mathbb{R}^{n_z}$ by finding the nearest neighbors in \mathcal{Z} for its each element \hat{z}_{ij} , to calculate the discrete representation $z^q \in \mathbb{R}^{h \times w \times n_z}$:

$$z_{ij}^q = \arg \min_{z_k \in \mathcal{Z}} (\|\hat{z}_{ij} - z_k\|_2), \quad (1)$$

where K denotes the size of the codebook and $i \in \{1, 2, \dots, H/8\}$, $j \in \{1, 2, \dots, W/8\}$ denote the coordinates in the feature space. The quantized PSF feature z^q is then applied to reconstruct the input PSF map \hat{I}_{PSF} by the VQVAE decoder G for self-supervised learning. The overall process is formulated as:

$$\hat{I}_{PSF} = G(z^q) = G(\mathcal{M}(E(I_{PSF}), \mathcal{Z})), \quad (2)$$

where \mathcal{M} is the feature matching process. Following (van den Oord et al., 2017), reconstruction loss and codebook loss are applied as the objective function \mathcal{L}_{VQ} for the training of PSF-VQVAE:

$$\mathcal{L}_{VQ}(E, G, \mathcal{Z}) = \|\hat{I}_{PSF} - I_{PSF}\|_1 + \|sg[\hat{z}] - z^q\|_2^2 + \|sg[z^q] - \hat{z}\|_2^2, \quad (3)$$

where $sg[\cdot]$ denotes stop gradient operation that addresses the non-differentiability of \mathcal{M} and facilitates the optimization of E and \mathcal{Z} , and β is set to 0.25 as a common practice.

Optical degradation network. Given that the PSF-VQVAE learns raw PSF features without modeling optical priors, we introduce ODN to further regularize LPR learning. ODN models the optical degradation process from a clear image to a degraded image, which is conditioned on the quantized PSF features z^q of the PSF-VQVAE to control the degradation pattern. An ODN encoder E_{ODN} , sharing the same architecture as E , is applied to map the clear image I_{clear} into latent space to obtain z_{clear} , which is fused with z^q by the ODN fusion module F_{ODN} to produce the PSFs-conditioned optical degradation features z_{OD} . The degraded image \hat{I}_{OD} is then reconstructed from z_{OD} by an ODN decoder G_{ODN} , where the objective function of ODN \mathcal{L}_{ODN} is computed between \hat{I}_{OD} and the ground truth degraded image I_{OD} . ODN and its training objective can be formulated as:

$$\hat{I}_{OD} = ODN(I_{clear}; z^q) = G_{ODN}(z_{OD}) = G_{ODN}(F_{ODN}(E_{OD}(I_{clear}), z^q)), \quad (4)$$

$$\mathcal{L}_{ODN}(E, \mathcal{Z}, E_{ODN}, G_{ODN}, F_{ODN}) = \|\hat{I}_{OD} - I_{OD}\|_1. \quad (5)$$

To this end, the LPR is achieved by jointly training the PSF-VQVAE and the ODN in an end-to-end manner, with the overall training objective given by:

$$\mathcal{L}_{LPR} = \mathcal{L}_{VQ} + \mathcal{L}_{ODN}. \quad (6)$$

Within LPR, optical priors are implicitly captured by the codebook and the ODN, which are subsequently leveraged to guide the prediction of latent PSF features from degraded images.

3.4 STAGE II: TRAINING A FOUNDATIONAL MODEL

Figure 3 (b) shows the established Foundational Computational Aberration Correction (FoundCAC) model guided by the pre-trained LPR. Considering that we aim to predict PSF features in latent space to guide CAC, FoundCAC mainly adopts an UNet architecture $\{E_{CAC}, G_{CAC}\}$ identical to that of VQVAE as the baseline model.

Latent PSF features prediction. To predict latent PSF features characterizing optical priors from degraded inputs I_{OD} , we employ an encoder E_{OD} identical to E_{CAC} constrained by the learned

LPR. The extracted features f_{PSF} are then matched with the pre-trained LPR codebook \mathcal{Z} to retrieve the corresponding PSF features f_{PSF}^q of I_{OD} . During training, the GT PSF map I_{PSF} is passed through the trained PSF-VQVAE to produce the GT LPR $z_{gt} = \mathcal{M}(E(I_{PSF}), \mathcal{Z})$ for supervising the predicted f_{PSF}^q based on feature matching loss \mathcal{L}_{FM} following (Chen et al., 2022a). Additionally, the trained ODN is applied to further regularize the prediction of f_{PSF}^q . Conditioning ODN on f_{PSF}^q , we degrade I_{clear} to \hat{I}_{OD} by ODN and compute the ODN loss \mathcal{L}_{ODN} of Equation 5 against I_{OD} . In this way, the training objective of LPR-guided latent PSF features prediction \mathcal{L}_{PFP} is the combination of codebook-guided \mathcal{L}_{FM} and ODN-guided \mathcal{L}_{ODN} :

$$\mathcal{L}_{PFP} = \mathcal{L}_{FM} + \mathcal{L}_{ODN}. \quad (7)$$

PSF-features-conditioned CAC network. The latent space of FoundCAC is conditioned on the predicted PSF features for leveraging the learned optical priors. We introduce a fusion module F_{CAC} that uses f_{PSF}^q to modulate the features f_{OD} extracted by E_{CAC} . We concatenate f_{PSF}^q with f_{OD} , and feed the results into several backbone blocks to perform deep fusion, yielding the computational aberration correction features f_{CAC} . The backbone can be initialized with any backbone in low-level vision, such as the classical RRDB (Wang et al., 2018) and Swin (Liang et al., 2021) blocks. Finally, G_{CAC} decodes f_{CAC} to reconstruct the correction result I_{CAC} . Similar to Chen et al. (2021a;b); Gong et al. (2024), we supervise I_{CAC} using an objective \mathcal{L}_{CAC} that combines fidelity and perceptual losses:

$$\mathcal{L}_{CAC} = \|I_{CAC} - I_{clear}\|_1 + \|\phi(I_{CAC}) - \phi(I_{clear})\|_2^2, \quad (8)$$

where ϕ is a pre-trained VGG-16 network (Simonyan & Zisserman, 2015). We do not discuss GAN or diffusion generative paradigms here, since the aberration correction task commonly focuses more on the modeling and learning of degradation patterns.

The entire FoundCAC model is trained end-to-end under the joint supervision of \mathcal{L}_{CAC} and \mathcal{L}_{PFP} . During this stage, only E_{CAC} , G_{CAC} , F_{CAC} , and E_{OD} are updated, while the parameters of the pre-trained codebook and ODN in LPR remain frozen.

4 EXPERIMENTS

4.1 IMPLEMENTATION DETAILS

Datasets. We sample $m_1 = 200$ and $m_2 = 3$ instances per class for AODLibpro `train` and AODLibpro `test`, yielding 3,600 training lenses and 54 test lenses with no overlap. For AODLibpro `train`, each lens randomly degrades 40 images from Flickr2K (Timofte et al., 2017) via a precise imaging simulator (Yang et al., 2024). For AODLibpro `test`, the degraded images are synthesized based on additional 26 collected clear images. Meanwhile, through manually designing and gathering open source designs, we construct a real-world lens aberration dataset *RealLens-Sim*, consisting of 4 minimalist optical systems with spherical or aspheric surfaces (MOS-A/S) (Jiang et al., 2024b), 1 metalens from Tseng et al. (2021)(MOS-Meta), one smartphone lens under 3 misalignment (MA) cases, and 2 high-end lenses including an ultra-wide lens and a smartphone lens (High-end). The same simulator is applied to simulate the paired images of them for numerical evaluation. For real-world cases, we collect real-snapped optical degradation images *RealLens-Snap* with fabricated single lenses, the commercial minimalist lens *CAYE 50mm f1/4*, two DSLRs of *Canon 24mm f1/4* and *Sony 18135*, and nano-optics data from Tseng et al. (2021).

Training details. On AODLibpro `train`, we first pre-train LPR for 100K iterations, and train the FoundCAC model for 200K iterations. Both training stages use 256×256 random crops with flips and rotations for data augmentation, with a batch size of 16. We use Adam with a learning rate of $2e-4$ to $1e-6$ decayed by a cosine annealing schedule. Training is conducted on two RTX 4090 GPUs, and inference uses a single RTX 4090. Consistent with Chen et al. (2022a), all encoders and decoders employ 3 groups of ResBlocks. For FoundCAC, we use 4 RSTB layers from Swin-T (Liang et al., 2021) as the deep fusion backbone, given its strong performance on spatial-varying OD (Jiang et al., 2024a). Ablations on alternative backbones are reported in Section 4.2 and 4.4.

In the following sections, we apply *RealLens* to evaluate the performance of blind aberration correction pipelines, and we further benchmark the model paradigms via AODLibpro `Test` with emphasis on the PSF representations. For more implementations, please refer to Appendix E and F.

4.2 BLIND CORRECTION FOR REAL-WORLD LENS ABERRATIONS

Numerical evaluation on *RealLens-Sim*. On the *RealLens-Sim*, we evaluate the overall capability of blind lens aberration correction methods to handle real-world aberrations as shown in Table 2. The suite includes the state-of-the-art deconvolution method fast two-step (Eboli et al., 2022), a universal Image Restoration (IR) model for real-world degradations represented by S3Diff (Zhang et al., 2024) trained under the BSRGAN (Zhang et al., 2021) data regime, and various LensLib-PT methods containing LensLibs of ZEBASELib (Gong et al., 2024), ZernikeLib (Jiang et al., 2024c), AODLib-LensNet (Côté et al., 2021), and AODLib-EAOD in OmniLens (Jiang et al., 2024b). For the LensLib-PT methods, we adopt SwinIR as the network architecture for its superior overall performance in OmniLens. In addition to our final FoundCAC trained on AODLibpro, we also report SwinIR trained on AODLibpro as a reference result.

Overall, our full framework achieves state-of-the-art blind aberration correction results, generalizing well across diverse real-world lens aberrations. OmniLens++ delivers pronounced gains on challenging aberration cases such as MOS-S/A and MOS-Meta, robustly handles highly stochastic misalignment aberrations, and surpasses fast two-step methods on high-end lens aberrations, which are specifically designed for them. Notably, a universal IR model trained without optical degradation data copes with the relatively mild aberrations of high-end lenses, yet struggles on more complex and severe cases, indicating the importance of dedicated research on lens aberration correction. Finally, the last three rows show that, atop the OmniLens baseline, AODLibpro and LPR yield average PSNR improvements of $0.71dB$ and $0.81dB$ respectively, verifying that both our data and model paradigm designs enhance the capacity of LensLib-PT-based pipeline for blind aberration correction. Additional visual results are provided in Appendix G.1.

Table 2: Comparison with potential blind lens aberration correction pipelines on *RealLens-Sim*. We report the PSNR/SSIM/LPIPS results under each sub-test-lenses-set. The latency of each method to process an image of 1920×1280 is also provided. The **best** and second results are highlighted.

Method	Latency (s)	<i>RealLens-Sim</i>				
		MOS-S/A	MOS-Meta	MA	High-end	Average
Fast two-step	0.390	20.65/0.712/0.3210	21.56/0.648/0.4596	<u>27.14</u> /0.765/0.1861	28.49/0.835/0.1650	24.46/0.740/0.2829
Universal IR model (S3Diff)	9.933	20.34/0.746/0.2615	21.36/0.687/0.4229	26.90/0.799/0.1779	29.69 /0.857/0.1423	24.57/0.772/0.2512
ZEBASELib-PT	0.782	23.09/0.791/0.2969	18.14/0.679/0.4931	25.91/0.837/0.1274	28.16/0.901/0.1053	23.83/0.802/0.2557
ZernikeLib-PT	0.782	24.41/0.822/0.1841	20.50/0.707/0.3806	25.16/0.850/0.1248	27.23/0.898/ 0.0932	24.33/0.819/0.1957
AODLib-LensNet-PT	0.782	23.10/0.796/0.2937	18.56/0.678/0.4993	25.97/0.858/0.1224	27.49/ 0.904 /0.0977	23.78/0.809/0.2533
AODLib-EAOD-PT	0.782	26.72/0.853/0.1597	<u>21.96</u> /0.748/0.3671	26.02/0.861/0.1015	27.72/0.903/0.0953	25.14/0.839/0.1842
AODLibpro-PT (SwinIR)	0.782	27.11 /0.862/0.1542	21.80/0.752/0.3441	26.69/ 0.866 /0.1035	27.81/ 0.904 /0.1006	<u>25.85</u> /0.846/0.1756
AODLibpro-PT (FoundCAC)	<u>0.417</u>	<u>27.09</u> /0.864/0.1465	23.32/0.769/0.3145	27.44/0.866/0.0982	28.81/0.904/0.0975	26.66 /0.851/0.1642

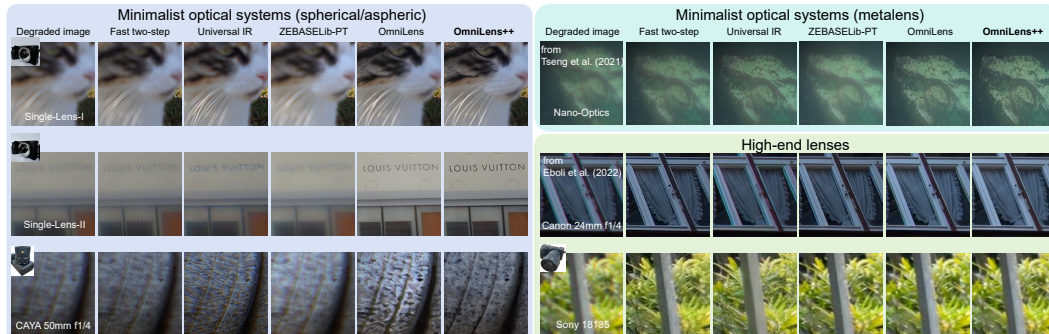


Figure 4: Visual results of representative blind lens aberration correction pipelines across real-world cases. More results and the capture details are provided in Appendix G.5 and G.6.

Qualitative evaluation on *RealLens-Snap*. Using real-snapped images (*RealLens-Snap*), we further conduct qualitative validation of the representative methods in Table 2, as shown in Figure 4. OmniLens++ shows clear advantages in minimalist lenses, reflected in better handling of blur, stronger suppression of purple fringing, and little introduction of artifacts and ringing. For out-of-domain metalens imaging results, our method successfully recovers a certain amount of high-frequency detail and removes most chromatic aberration. Finally, similar to the fast two-step method, OmniLens++ also improves the image quality of high-end DSLR lenses by enhancing

sharpness and correcting purple fringing. In summary, OmniLens++ exhibits strong generalization capacity for blind aberration correction on real-snapped images.

Table 3: Comparison with state-of-the-art networks in CAC on AODLibpro `test` benchmark. The **best** and **second** results are highlighted.

Network	Latency (s)	PSNR	SSIM	LPIPS
RRDBNet	0.296	27.22	0.852	0.1519
SwinIR	0.782	28.29	0.871	0.1346
MIMOUNet	0.405	28.11	0.874	0.1651
NAFNet	0.353	27.48	0.866	0.2078
Restormer	1.859	27.11	0.867	0.1430
X-Restormer	2.797	28.11	0.870	0.1408
PromptIR	2.063	27.14	0.869	0.1404
DiffBIR	66.130	27.52	0.833	0.1430
S3Diff	9.933	23.10	0.762	0.1678
FOVKPN	0.166	27.23	0.851	0.1586
DFUnet	0.137	27.04	0.841	0.1639
FoundCAC (RRDB)	0.330	26.63	0.858	0.1409
FoundCAC (Swin)	0.417	28.67	0.873	0.1277

Table 4: Comparison between LPR and other potential representations for PSFs. We employ the same fusion module as LPR for all the PSF features (the same is true for the experiments in Table 1).

Representation	PSNR	SSIM	LPIPS
Baseline	26.10	0.837	0.1701
GT-PSFs-guided (SFR)	28.73	0.873	0.1269
GT-PSFs-guided (Downsample)	28.20	0.861	0.1315
PSFs prediction	28.25	0.861	0.1283
PSFs feature prediction	28.42	0.867	0.1287
ODN	28.40	0.864	0.1273
PSF-VQVAE	28.55	0.868	0.1293
+CAC	26.95	0.862	0.1346
+ODN (LPR)	28.67	0.873	0.1277
+CAC+ODN	26.76	0.861	0.1395

4.3 EFFECTIVENESS OF FOUNDATION CAC MODEL AND LPR

Comparison with state-of-the-art networks for blind CAC. We fix the training set to AODLibpro `train` and evaluate on the AODLibpro `test` benchmark, comparing FoundCAC against state-of-the-art blind CAC networks (Wang et al., 2018; Liang et al., 2021; Cho et al., 2021; Chen et al., 2022b; Zamir et al., 2022; Chen et al., 2024; Potlapalli et al., 2023; Lin et al., 2024; Zhang et al., 2024; Chen et al., 2021a;b) in Table 3. We also report a CNN version of FoundCAC that adopts RRDB as the deep fusion backbone. Compared with their respective baselines, FoundCAC using RRDB and RSTB as backbones shows better correction performance without a noticeable increase in inference time. This indicates the effectiveness of our LPR-guided model paradigm and its applicability across multiple backbone architectures. Meanwhile, with RSTB as the backbone, which is suited for spatial-varying optical degradation, FoundCAC achieves state-of-the-art results on the benchmark. PromptIR shows limited improvement over its baseline Restormer, suggesting that the class-based prompt is not appropriate for representing optical degradation priors. Finally, diffusion-based methods perform poorly on diverse degradation patterns with a clear disadvantage in latency. This verifies that for aberration correction, learning optical priors is more effective than injecting clear image priors. Furthermore, the representation of optical priors enables FoundCAC to outperform methods with specialized network designs for optical degradation (FOVKPN and DFUnet).

Comparison with potential PSF representations. In Table 4, we further explore how to learn a better latent PSF representation. First, preparing PSF maps in the form of SFR is a better choice than downsampling in Jiang et al. (2024a). With this setup, constraining with PSF-VQVAE or with ODN individually yields better guidance for latent PSF features prediction than direct supervision on PSFs or their features, validating both designs. Their combination achieves the best performance by leveraging the ability of the VQ strategy to store feature vectors and the advantage of ODN in modeling optical priors. In addition, we compare another potential solution that constrains the latent space of the PSF-VQVAE directly with the CAC task. The CAC subtask, either alone or with ODN, fails to induce effective PSF representations. Overall, LPR that combines PSF-VQVAE and ODN provides more effective guidance to aberration correction than alternative representations.

4.4 ABLATION STUDIES

We perform ablations to investigate the individual effectiveness of AODLibpro and LPR, and their interaction within OmniLens++. To ensure fairness, any experiment that modifies the training data is tested on *RealLens-Sim* to assess the overall framework, while models trained on the full AODLibpro `train` are evaluated on the AODLibpro `test` to evaluate the model paradigm.

Evaluation of AODLibpro. We train a SwinIR model under different LensLib settings to verify their performance. Table 5 shows that incorporating additional design specifications that we considered can improve the quality of LensLib. The results in Table 6 indicate that, compared with the RMS-based sampling basis, the proposed OIQ and OD-Class yield models of stronger generalization ability, and combining them contributes to a more comprehensive improvement. We further demonstrate the advantages of AODLibpro over its baseline AODLib-EAOD in Figure 5. Benefiting from

Table 5: Ablations on design specifications. A.S.: Aspheric Surface. I.P.P: Image Plane Perturbation.

Specification	PSNR	LPIPS
Baseline in OmniLens	25.95	0.1897
+ A.S.	25.72	0.1893
+ A.S.&I.P.P.	25.85	0.1756

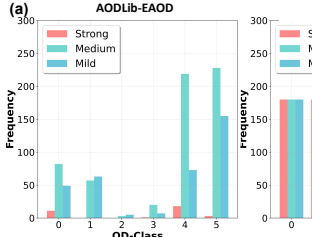


Table 6: Ablations on sampling basis.

Sampling basis	PSNR	LPIPS
RMS	25.56	0.1843
OIQ	26.10	0.1859
OD-Class	25.85	0.1815
Hybrid	25.85	0.1756

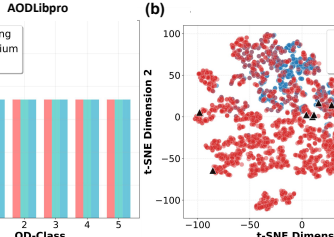


Table 7: Ablations on components of LPR guidance.

	E_{OD}	Fusion	PSNR	LPIPS
Baseline	✗	✗	26.10	0.1701
1	✓	✗	25.43	0.1675
2	✗	RRDB	26.42	0.1466
3	✓	RRDB	26.63	0.1409
4	✗	Swin	28.46	0.1318
5	✓	Swin	28.67	0.1277

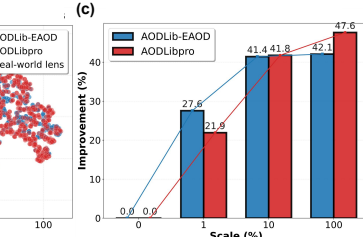


Figure 5: AODLibpro v.s. AODLib-EAOD in terms of uniformity of aberration distributions, coverage over real-world lenses, and scalability. (a) Histogram of degradation type distributions in the sampled lenses. (b) LensLib coverage visualization based on OIQ evaluated per FoV and wavelength. (c) Improvements of SwinIR trained with LensLibs of different scales over the method without LensLib (Eboli et al., 2022). The improvement is averaged across the PSNR and LPIPS.

specification expansion and the hybrid sampling basis, the samples in AODLibpro are uniformly distributed across degradation severity and spatial variation patterns (Figure 5 (a)), while the overall aberration distribution is broader and can cover all of the lens samples in *RealLens-Sim* (Figure 5 (b)). These advantages are conducive to the scalability of AODLibpro, where significant gains are brought by increasing the data scale (Figure 5 (c)), addressing the limitations of AODLib-EAOD.

Evaluation of components for LPR guidance. As shown in Table 7, starting from the UNet baseline, we evaluate the effectiveness of the predicted latent PSF features and the proposed fusion module. Settings 1, 3, and 5 show that both CNN-based and Transformer-based fusion enable LPR to provide effective guidance, yielding PSNR gains of $0.32 \sim 2.57dB$. Meanwhile, the deep fusion backbone is necessary because simply adding the predicted latent PSF features yields limited improvements, indicating that the model requires considerable parameters to learn the interaction between optical priors and image features. The comparisons between settings 2 and 3, and between 4 and 5, further show that the effective guidance of LPR is not due to the additional parameters; under the same backbone, incorporating the latent PSF features contributes to significant gains.

Table 8: Improvements brought by LPR under different data scales of AODLibpro.

LPR	Scale: 1%		Scale: 10%		Scale: 100%	
	PSNR	LPIPS	PSNR	LPIPS	PSNR	LPIPS
✗	23.82	0.2187	25.23	0.1998	25.92	0.1881
✓	23.39 ($\downarrow 10.41\%$)	0.2363 ($\downarrow 8.05\%$)	25.72 ($\uparrow 10.67\%$)	0.1782 ($\uparrow 10.81\%$)	26.66 ($\uparrow 15.67\%$)	0.1642 ($\uparrow 12.71\%$)

Effectiveness of LPR under different data scales. We investigate whether the proposed LPR-guided model paradigm can exploit the potential of the enlarged AODLibpro in Table 8. With 1% data, LPR fails to learn effective PSF representations and produces negative gains. This is anticipated, as the codebook captures only a limited set of PSF features, which prevents reliable retrieval for unseen real-world distributions. Scaling the data alleviates this and enables LPR to provide effective guidance. As data scale increases, LPR delivers larger improvements over the baseline, indicating that it effectively leverages the enhanced scalability of AODLibpro.

5 CONCLUSION AND FUTURE WORK

Conclusion. We present OmniLens++ as a robust blind aberration correction solution under the LensLib-PT paradigm. AODLibpro improves coverage and scalability on the data side, and LPR provides the first PSF-guided model paradigm that preserves the blind setting. OmniLens++ generalizes across diverse real-world aberrations, which is comparable to the state-of-the-art deconvolution-based method on mild high-end lens aberrations, and excels on severe aberrations in minimalist optical systems, positioning it as a promising general solution for blind aberration correction.

Future work. Looking ahead, benefiting from the scalability of AODLibpro, future work will focus on extending it with metasurfaces and diffractive optical elements for stronger generalization. Then, building on the OmniLens++ framework, we will further investigate aberration correction under degradations coupled with optics including depth of field (Abuolaim & Brown, 2020; Ruan et al., 2022; Yang et al., 2023; 2025), under display imaging (Feng et al., 2021; Wang et al., 2024), low light conditions (Liu et al., 2023), and sensor noise (Zheng et al., 2025) to support real-world deployment. Last but not least, we believe it is important to exploit FoundCAC as a pretrained model, where a flexible fine-tuning pipeline is urged to enhance its practical value.

REFERENCES

Abdullah Abuolaim and Michael S Brown. Defocus deblurring using dual-pixel data. In *ECCV*, 2020. 11

Yuang Ai, Huaibo Huang, Xiaoqiang Zhou, Jieyang Wang, and Ran He. Multimodal prompt perceiver: Empower adaptiveness generalizability and fidelity for all-in-one image restoration. In *CVPR*, 2024. 3

Chaofeng Chen, Xinyu Shi, Yipeng Qin, Xiaoming Li, Xiaoguang Han, Tao Yang, and Shihui Guo. Real-world blind super-resolution via feature matching with implicit high-resolution priors. In *MM*, 2022a. 7, 18

Liangyu Chen, Xiaojie Chu, Xiangyu Zhang, and Jian Sun. Simple baselines for image restoration. In *ECCV*, 2022b. 9

Liqun Chen, Yuxuan Li, Jun Dai, Jinwei Gu, and Tianfan Xue. A physics-informed blur learning framework for imaging systems. In *CVPR*, 2025. 2, 3

Shiqi Chen, Huajun Feng, Keming Gao, Zhihai Xu, and Yuetong Chen. Extreme-quality computational imaging via degradation framework. In *ICCV*, 2021a. 3, 7, 9, 20

Shiqi Chen, Huajun Feng, Dexin Pan, Zhihai Xu, Qi Li, and Yuetong Chen. Optical aberrations correction in postprocessing using imaging simulation. *ACM Transactions on Graphics*, 2021b. 2, 3, 5, 7, 9, 20

Shiqi Chen, Jingwen Zhou, Menghao Li, Yuetong Chen, and Tingting Jiang. Mobile image restoration via prior quantization. *Pattern Recognition Letters*, 2023. 2, 3, 4, 6

Xiangyu Chen, Zheyuan Li, Yuandong Pu, Yihao Liu, Jiantao Zhou, Yu Qiao, and Chao Dong. A comparative study of image restoration networks for general backbone network design. In *ECCV*, 2024. 9

Sung-Jin Cho, Seo-Won Ji, Jun-Pyo Hong, Seung-Won Jung, and Sung-Jea Ko. Rethinking coarse-to-fine approach in single image deblurring. In *ICCV*, 2021. 9

Geoffroi Côté, Jean-François Lalonde, and Simon Thibault. Deep learning-enabled framework for automatic lens design starting point generation. *Optics Express*, 2021. 8, 22

Thomas Eboli, Jean-Michel Morel, and Gabriele Facciolo. Fast two-step blind optical aberration correction. In *ECCV*, 2022. 2, 3, 8, 10, 20, 21, 22

Patrick Esser, Robin Rombach, and Björn Ommer. Taming transformers for high-resolution image synthesis. In *CVPR*, 2021. 4, 18

Ruicheng Feng, Chongyi Li, Huaijin Chen, Shuai Li, Chen Change Loy, and Jinwei Gu. Removing diffraction image artifacts in under-display camera via dynamic skip connection network. In *CVPR*, 2021. 11

Jin Gong, Runzhao Yang, Weihang Zhang, Jinli Suo, and Qionghai Dai. A physics-informed low-rank deep neural network for blind and universal lens aberration correction. In *CVPR*, 2024. 2, 3, 7, 8, 20, 22

Felix Heide, Mushfiqur Rouf, Matthias B. Hullin, Björn Labitzke, Wolfgang Heidrich, and Andreas Kolb. High-quality computational imaging through simple lenses. *ACM Transactions on Graphics*, 2013. [2](#)

JiaKui Hu, Lujia Jin, Zhengjian Yao, and Yanye Lu. Universal image restoration pre-training via degradation classification. In *ICLR*, 2025. [2](#), [3](#)

Lejia Hu, Shuwen Hu, Wei Gong, and Ke Si. Image enhancement for fluorescence microscopy based on deep learning with prior knowledge of aberration. *Optics Letters*, 2021. [3](#)

Junjun Jiang, Zengyuan Zuo, Gang Wu, Kui Jiang, and Xianming Liu. A survey on all-in-one image restoration: Taxonomy, evaluation and future trends. *IEEE Transactions on Pattern Analysis and Machine Intelligence*, 2025a. [3](#)

Qi Jiang, Shaohua Gao, Yao Gao, Kailun Yang, Zhonghua Yi, Hao Shi, Lei Sun, and Kaiwei Wang. Minimalist and high-quality panoramic imaging with PSF-aware transformers. *IEEE Transactions on Image Processing*, 2024a. [2](#), [3](#), [7](#), [9](#), [16](#)

Qi Jiang, Yao Gao, Shaohua Gao, Zhonghua Yi, Xiaolong Qian, Hao Shi, Kailun Yang, Lei Sun, and Kaiwei Wang. OmniLens: Towards universal lens aberration correction via lenslib-to-specific domain adaptation. *arXiv preprint arXiv:2409.05809*, 2024b. [2](#), [3](#), [4](#), [5](#), [7](#), [8](#), [20](#), [22](#)

Qi Jiang, Hao Shi, Shaohua Gao, Jiaming Zhang, Kailun Yang, Lei Sun, Huajian Ni, and Kaiwei Wang. Computational imaging for machine perception: Transferring semantic segmentation beyond aberrations. *IEEE Transactions on Computational Imaging*, 2024c. [3](#), [8](#), [22](#)

Qi Jiang, Zhonghua Yi, Shaohua Gao, Yao Gao, Xiaolong Qian, Hao Shi, Lei Sun, JinXing Niu, Kaiwei Wang, Kailun Yang, and Jian Bai. Representing domain-mixing optical degradation for real-world computational aberration correction via vector quantization. *Optics & Laser Technology*, 2025b. [4](#)

Neel Joshi, Richard Szeliski, and David J Kriegman. PSF estimation using sharp edge prediction. In *CVPR*, 2008. [4](#)

Eric Kee, Sylvain Paris, Simon Chen, and Jue Wang. Modeling and removing spatially-varying optical blur. In *ICCP*, 2011. [3](#)

Boyun Li, Xiao Liu, Peng Hu, Zhongqin Wu, Jiancheng Lv, and Xi Peng. All-in-one image restoration for unknown corruption. In *CVPR*, 2022. [3](#)

Xiu Li, Jinli Suo, Weihang Zhang, Xin Yuan, and Qionghai Dai. Universal and flexible optical aberration correction using deep-prior based deconvolution. In *ICCV*, 2021. [3](#)

Jie Liang, Radu Timofte, Qiaosi Yi, Shuaizheng Liu, Lingchen Sun, Rongyuan Wu, Xindong Zhang, Hui Zeng, Lei Zhang, Yibin Huang, et al. NTIRE 2024 restore any image model (RAIM) in the wild challenge. In *CVPRW*, 2024. [16](#)

Jingyun Liang, Jiezhang Cao, Guolei Sun, Kai Zhang, Luc Van Gool, and Radu Timofte. SwinIR: Image restoration using swin transformer. In *ICCVW*, 2021. [7](#), [9](#), [19](#)

Ting Lin, Shiqi Chen, Huijun Feng, Zhihai Xu, Qi Li, and Yueling Chen. Non-blind optical degradation correction via frequency self-adaptive and finetune tactics. *Optics Express*, 2022. [2](#), [3](#)

Xinqi Lin, Jingwen He, Ziyan Chen, Zhaoyang Lyu, Bo Dai, Fanghua Yu, Yu Qiao, Wanli Ouyang, and Chao Dong. DiffBIR: Toward blind image restoration with generative diffusion prior. In *ECCV*, 2024. [9](#)

Haibin Liu, Wenyong Li, Shaohua Gao, Qi Jiang, Lei Sun, Benhao Zhang, Liefeng Zhao, Jiahuang Zhang, and Kaiwei Wang. Application of deep learning in active alignment leads to high-efficiency and accurate camera lens assembly. *Optics Express*, 2024. [2](#)

Yunlong Liu, Tao Huang, Weisheng Dong, Fangfang Wu, Xin Li, and Guangming Shi. Low-light image enhancement with multi-stage residue quantization and brightness-aware attention. In *ICCV*, 2023. [11](#)

Jun Luo, Yunfeng Nie, Wenqi Ren, Xiaochun Cao, and Ming-Hsuan Yang. Correcting optical aberration via depth-aware point spread functions. *IEEE Transactions on Pattern Analysis and Machine Intelligence*, 2024. 3

Jiaqi Ma, Tianheng Cheng, Guoli Wang, Qian Zhang, Xinggang Wang, and Lefei Zhang. ProRes: Exploring degradation-aware visual prompt for universal image restoration. *arXiv preprint arXiv:2306.13653*, 2023. 3

Anish Mittal, Rajiv Soundararajan, and Alan C. Bovik. Making a “completely blind” image quality analyzer. *IEEE Signal Processing Letters*, 2013. 27

Yifan Peng, Qilin Sun, Xiong Dun, Gordon Wetzstein, Wolfgang Heidrich, and Felix Heide. Learned large field-of-view imaging with thin-plate optics. *ACM Transactions on Graphics*, 2019. 2

Vaishnav Potlapalli, Syed Waqas Zamir, Salman H. Khan, and Fahad Shahbaz Khan. PromptIR: Prompting for all-in-one image restoration. In *NeurIPS*, 2023. 2, 3, 9

Xiaolong Qian, Qi Jiang, Yao Gao, Shaohua Gao, Zhonghua Yi, Lei Sun, Kai Wei, Haifeng Li, Kailun Yang, Kaiwei Wang, and Jian Bai. Towards single-lens controllable depth-of-field imaging via depth-aware point spread functions. *IEEE Transactions on Computational Imaging*, 2025. 3

Joshua D. Rego, Karthik Kulkarni, and Suren Jayasuriya. Robust lensless image reconstruction via PSF estimation. In *WACV*, 2021. 4

Lingyan Ruan, Bin Chen, Jizhou Li, and Miuling Lam. Learning to deblur using light field generated and real defocus images. In *CVPR*, 2022. 11

Christian J. Schuler, Michael Hirsch, Stefan Harmeling, and Bernhard Schölkopf. Non-stationary correction of optical aberrations. In *ICCV*, 2011. 2

Christian J. Schuler, Michael Hirsch, Stefan Harmeling, and Bernhard Schölkopf. Blind correction of optical aberrations. In *ECCV*, 2012. 2, 3

Karen Simonyan and Andrew Zisserman. Very deep convolutional networks for large-scale image recognition. In *ICLR*, 2015. 7

Qilin Sun, Congli Wang, Qiang Fu, Xiong Dun, and Wolfgang Heidrich. End-to-end complex lens design with differentiate ray tracing. *ACM Transactions on Graphics*, 2021. 16

Radu Timofte, Eirikur Agustsson, Luc Van Gool, Ming-Hsuan Yang, Lei Zhang, Bee Lim, Sanghyun Son, Heewon Kim, Seungjun Nah, Kyoung Mu Lee, et al. NTIRE 2017 challenge on single image super-resolution: Methods and results. In *CVPRW*, 2017. 7

Ethan Tseng, Shane Colburn, James Whitehead, Luocheng Huang, Seung-Hwan Baek, Arka Majumdar, and Felix Heide. Neural nano-optics for high-quality thin lens imaging. *Nature Communications*, 2021. 3, 7, 21

Aäron van den Oord, Oriol Vinyals, and Koray Kavukcuoglu. Neural discrete representation learning. In *NeurIPS*, 2017. 2, 4, 6

Jian Wang, Sizhuo Ma, Karl Bayer, Yi Zhang, Peihao Wang, Bing Zhou, Shree Nayar, and Gurunandan Krishnan. Perspective-aligned ar mirror with under-display camera. *ACM Transactions on Graphics*, 2024. 11

Jianyi Wang, Kelvin CK Chan, and Chen Change Loy. Exploring CLIP for assessing the look and feel of images. In *AAAI*, 2023. 27

Xintao Wang, Ke Yu, Shixiang Wu, Jinjin Gu, Yihao Liu, Chao Dong, Yu Qiao, and Chen Change Loy. ESRGAN: Enhanced super-resolution generative adversarial networks. In *ECCVW*, 2018. 7, 9, 19

Zhou Wang, Alan C. Bovik, Hamid R. Sheikh, and Eero P. Simoncelli. Image quality assessment: from error visibility to structural similarity. *IEEE Transactions on Image Processing*, 2004. 16

Shijie Wei, Huachao Cheng, Ben Xue, Xihang Yang, Yinpeng Ma, Yue Wang, Teli Xi, and Xiaopeng Shao. Computational imaging-based single-lens imaging systems and performance evaluation. *Optics Express*, 2024. 3

Sidi Yang, Tianhe Wu, Shuwei Shi, Shanshan Lao, Yuan Gong, Mingdeng Cao, Jiahao Wang, and Yujiu Yang. MANIQA: Multi-dimension attention network for no-reference image quality assessment. In *CVPRW*, 2022. 27

Xinge Yang, Qiang Fu, Mohamed Elhoseiny, and Wolfgang Heidrich. Aberration-aware depth-from-focus. *IEEE Transactions on Pattern Analysis and Machine Intelligence*, 2023. 11

Xinge Yang, Matheus Souza, Kunyi Wang, Praneeth Chakravarthula, Qiang Fu, and Wolfgang Heidrich. End-to-end hybrid refractive-diffractive lens design with differentiable ray-wave model. *arXiv preprint arXiv:2406.00834*, 2024. 7, 15, 19

Xinge Yang, Chuong Nguyen, Wenbin Wang, Kaizhang Kang, Wolfgang Heidrich, and Xiaoxing Li. Efficient depth-and spatially-varying image simulation for defocus deblur. *arXiv preprint arXiv:2507.00372*, 2025. 11

Kyrollos Yanny, Kristina Monakhova, Richard W. Shuai, and Laura Waller. Deep learning for fast spatially varying deconvolution. *Optica*, 2022. 3

Tao Yue, Jinli Suo, Jue Wang, Xun Cao, and Qionghai Dai. Blind optical aberration correction by exploring geometric and visual priors. In *CVPR*, 2015. 3

Syed Waqas Zamir, Aditya Arora, Salman Khan, Munawar Hayat, Fahad Shahbaz Khan, and Ming-Hsuan Yang. Restormer: Efficient transformer for high-resolution image restoration. In *CVPR*, 2022. 9

Aiping Zhang, Zongsheng Yue, Renjing Pei, Wenqi Ren, and Xiaochun Cao. Degradation-guided one-step image super-resolution with diffusion priors. *arXiv preprint arXiv:2409.17058*, 2024. 8, 9, 22

Kai Zhang, Jingyun Liang, Luc Van Gool, and Radu Timofte. Designing a practical degradation model for deep blind image super-resolution. In *ICCV*, 2021. 8

Xu Zhang, Jiaqi Ma, Guoli Wang, Qian Zhang, Huan Zhang, and Lefei Zhang. Perceive-IR: Learning to perceive degradation better for all-in-one image restoration. *IEEE Transactions on Image Processing*, 2025. 3

Amber Yijia Zheng, Yu Zhang, Jun Hu, Raymond A. Yeh, and Chen Chen. DarkDiff: Advancing low-light raw enhancement by retasking diffusion models for camera ISP. *arXiv preprint arXiv:2505.23743*, 2025. 11

Jingwen Zhou, Shiqi Chen, Zheng Ren, Wenguan Zhang, Jiapu Yan, Huajun Feng, Qi Li, and Yuet-ting Chen. Revealing the preference for correcting separated aberrations in joint optic-image design. *Optics and Lasers in Engineering*, 2024. 2, 4

A STATEMENT

Ethics statement. We explore a robust blind aberration correction framework to address lens aberrations of arbitrary lenses, which is valuable for the applications of light-weight optical systems with uncorrected aberrations. This technology will facilitate the development of various mobile and wearable devices, such as mobile cameras, intelligent robots, and AR/VR equipment. However, the advantage of the tiny size of light-weight optical systems may also be leveraged for military reconnaissance and sneak shots. We hope that the relevant applications can be regularized by laws to prevent misuse.

Reproducibility statement. We state that the OmniLens++ framework is highly reproducible. At the data level, the specific specification settings, sampling basis, and OD image preparation details are presented in Section 3.2 and Appendix D, F.1, and the simulation component directly uses the open source DeepLens (Yang et al., 2024) repository. At the model level, Section 3.3 describes feature processing at each key node in detail, and the exact forms of all loss functions are provided. Appendix E also presents the specific network architectures and parameter settings for each stage of FoundCAC. Upon publication, all source code and data (lens design files, simulated and real-snapped OD images) will be released. Together with the detailed descriptions in the paper, the entire OmniLens++ framework can be well reproduced.

Large language model statement. We employed a large language model tool for language editing only, such as improving fluency, tightening long sentences, and refining phrasing to achieve a more native-like expression. All technical claims, methods, and results were written, verified, and approved by the authors, who assume full responsibility for the final manuscript.

B ILLUSTRATION OF ABBREVIATIONS

Due to some lengthy proper terms, this paper uses and defines many abbreviations. Table 9 summarizes all abbreviations along with their full forms to facilitate quick reference. In this appendix, we additionally abbreviate Optical Degradation (OD) and Computational Aberration Correction (CAC) for ease of expression.

Table 9: Illustration of abbreviations.

Abbreviation	Explanation
OD	Optical Degradation
FoV	Field of View
CAC	Computational Aberration Correction
PSF	Point Spread Function
LensLib-PT	Lens Library Pre-Training
FoundCAC	Foundational CAC
AOD	Automatic Optical Design
EAOD	Evolution-based Automatic Optical Design
OIQ	Optical Image Quality
OD-Class	Optical Degradation Distribution Category
LPR	Latent PSF Representation
ODN	Optical Degradation Network
GT	Ground Truth
IR	Image Restoration
MOS	Minimalist Optical System
RSTB	Residual Swin Transformer Block
RRDB	Residual in Residual Dense Block

C DETAILED SETTINGS FOR EXPERIMENTS IN MOTIVATION

The schematic diagrams of the model paradigms in Table 1 of Section 3.1 are shown in Figure 6. All encoders and decoders use the same design as in the final FoundCAC, namely 3 groups of ResBlocks. All fusions between PSF features and image features adopt F_{CAC} , that is, concatenation followed by deep feature backbones of 4 RSTB layers. Supervision for both PSFs prediction and PSFs features prediction applies L1 loss. Other training settings follow those of the CAC stage in

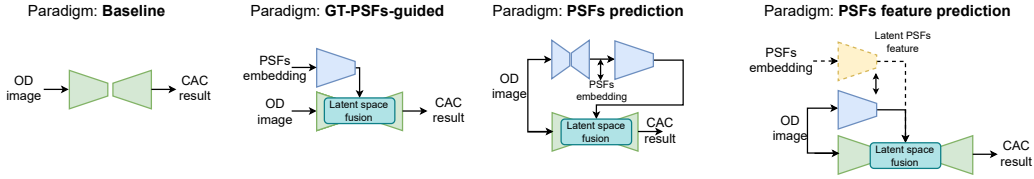


Figure 6: Illustration of the model paradigms in motivation.

FoundCAC. Additionally, all models in this table are trained on AODLibpro-Train and evaluated on the AODLibpro-Test benchmark to evaluate network performance.

D DETAILS FOR AODLIBPRO CONSTRUCTION

D.1 DETAILS FOR SUPPLEMENTED SPECIFICATIONS

Definition of the aspheric surface. The aspheric lens surface is an optical surface whose curvature deviates from a constant-radius sphere. Unlike conventional spherical surfaces, its profile is mathematically defined by higher-order polynomials, enabling precise control over light refraction across the entire aperture. The height of a standard aspheric surface [Sun et al. \(2021\)](#) is defined as a function of the radial distance r :

$$h(r) = \frac{cr^2}{1 + \sqrt{1 - (1 + \kappa)c^2r^2}} + \sum_{i=2}^{N_A} a_{2i}r^{2i}, \quad (9)$$

where c denotes the curvature, κ is the conic coefficient, a_{2i} 's are higher-order coefficients, and N_A defines the highest-order aspheric coefficient.

Image distance perturbation constrained by depth of field. We constrain the image distance perturbation amplitude within acceptable limits using the Depth of Field (DoF) formula:

$$\Delta L = \Delta L_1 + \Delta L_2 = \frac{F\delta L^2}{f^2 + F\delta L} + \frac{F\delta L^2}{f^2 - F\delta L}, \quad (10)$$

where δ is the permissible circle of confusion diameter, f is the lens focal length, F is the F-number, L is the image distance, ΔL_1 is the near DoF, and ΔL_2 is the far DoF. Image distance perturbation range is constrained within $[-\Delta L_1, \Delta L_2]$, and δ is set to $24\mu\text{m}$ in this work. The perturbation probability γ is set to 25% empirically.

D.2 DETAILS FOR HYBRID SAMPLING BASIS

Calculation of OIQ. OIQ incorporates traditional fidelity-based image quality metrics (PSNR and SSIM ([Wang et al., 2004](#))) as well as the SFR-based metric to provide an image quality assessment considering optical properties:

$$OIQ = \lambda_1 \frac{PSNR}{50} + \lambda_2 \frac{SSIM - 0.5}{0.5} + \lambda_3 OIQE, \quad (11)$$

where PSNR and SSIM are processed following ([Liang et al., 2024](#)) to obtain normalized metrics, while SFR is represented as OIQE ([Jiang et al., 2024a](#)), which denotes the ratio of the SFR of the evaluated target to that of a lens without OD. The weights are set to $\lambda_1 = 0.4$, $\lambda_2 = 0.3$, $\lambda_3 = 0.3$ to control the value ranges so that the 3 normalized metrics are close in range following ([Liang et al., 2024](#)).

Definition of OD severity category. The average OIQ across the 5 knife-edge image patches of different FoVs is calculated to represent the overall severity level of the target lens's OD. The average OIQ lies within $[0, 1]$, where a larger value indicates lower overall OD severity (higher optical image quality). Therefore, we divide the range into 3 intervals to categorize different OD severity levels for sampling, as shown in Figure 7.

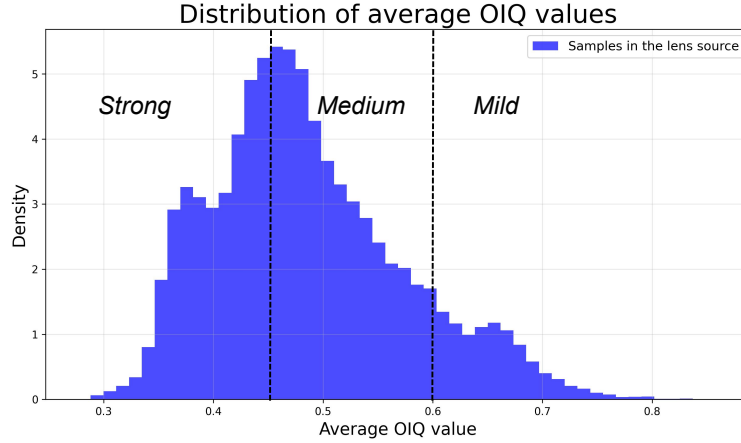


Figure 7: Illustration of the definition for OD severity category.

Calculation of the spatial uniformity. We first define the coefficient of variation (CV) from the variance and mean of OIQ across the 5 FoVs, then use it to compute a spatial uniformity metric U_S that measures the uniformity of the OD spatial distribution:

$$CV = \frac{Std(\{OIQ_i|i = 1, \dots, 5\})}{Avg(\{OIQ_i|i = 1, \dots, 5\})}, \quad (12)$$

$$U_S = e^{-5CV}, \quad (13)$$

where OIQ_i is the OIQ of the i^{th} FoV. A larger U_S indicates that the OD spatial distribution of the lens is more uniform.

OD-Class	U_S	OIQ trend	Classification criteria	Descriptions
0	$U_S > \alpha$		$U_S > \alpha$	Spatial-uniform
1	$U_S < \alpha$		$U_S < \alpha, \text{all } \text{Diff}(OIQ) < 0$	OIQ monotonically decreases, and OD becomes progressively more severe from the central FoV toward the periphery.
2	$U_S > \alpha$		$U_S < \alpha, \text{min_idx}(OIQ) = 1$	OD is most severe at the central FoV, that is, the minimum OIQ occurs at the "1" FoV (including the case where OIQ increases monotonically).
3	$U_S > \alpha$		$U_S < \alpha, \text{min_idx}(OIQ) = 2/3/4$	OD is most severe in the middle three FoV, that is, the minimum OIQ occurs at FoV "1", "2", or "3".
4	$U_S > \alpha$		$U_S < \alpha, \text{min_idx}(OIQ) = 5, \text{max_idx}(OIQ) = 1$	OD is most severe at the peripheral FoV and mildest at the center (unlike the monotonically decreasing case, the OIQ across the three middle FoVs is non-monotonic).
5	$U_S > \alpha$		$U_S < \alpha, \text{min_idx}(OIQ) = 5, \text{max_idx}(OIQ) \neq 1$	OD is most severe at the peripheral FoV and not mildest at the center.

We set $\alpha = 0.85$ empirically.

$\text{all } \text{Diff}(OIQ) < 0$: The first order difference of the OIQ vector is strictly positive.

$\text{min_idx}(OIQ)/\text{max_idx}(OIQ)$: The FoV index at which the minimum/maximum OIQ occurs.

Figure 8: Illustration of the definition of OD-Class. Notably, for cases where OD is most severe at the peripheral FoV, we define OD-Classes "4" and "5" because we observe that some lenses, despite showing the most severe OD at the peripheral FoV, also exhibit relatively severe OD at the center FoV. This OD pattern clearly differs from the typical OD pattern of a sharp center and blurred edge, which should be independently considered.

Definition of OD-Class. Figure 8 provides detailed definitions for each OD-Class, including the U_S value range, schematic OIQ trend plots, classification criteria, and supplementary descriptions. This basis allows any OIQ to fall into one class, enabling the classification and description of all possible OD patterns. To the best of our knowledge, there is currently no such detailed categorization of OD distribution patterns, so we make a preliminary attempt to explore this problem here. Table 6 shows that using the proposed OD-Class for sampling can construct a more effective LensLib. We hope this classification approach can provide new insights for this field to understand OD distribution patterns.

Discussion on chromatic aberrations. We do not include chromatic aberration as a criterion in OD classification because preliminary experiments show that it has little impact on the final CAC results, as shown in Figure 9. Using the same computation pipeline as U_S , we compute the channel-wise uniformity of OIQ to quantify the severity of chromatic aberration and divide it into 5 categories, where a smaller category index indicates more severe chromatic aberration. The distribution of chromatic aberration in AODLibpro Test is shown in Figure 9 (a). We tally the performance of our trained FoundCAC at different chromatic levels and find no obvious pattern in its performance as the severity of chromatic aberration changes, as shown in Figure 9 (b). This indicates that chromatic aberration has little effect on CAC models trained on LensLib, even though it is an often-discussed OD pattern. Meanwhile, our experiments also include cases with pronounced chromatic aberration, as in Figure 4, where our method effectively suppresses purple fringing caused by chromatic aberration. These evidences indicate that although chromatic aberration is not considered in data sampling, it does not affect the model’s performance in this respect.

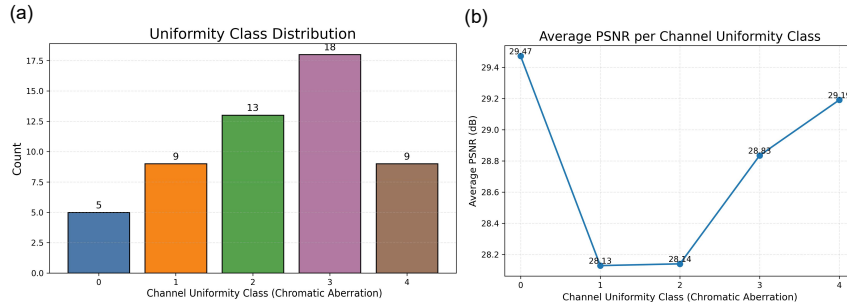


Figure 9: Evidence for omitting the chromatic aberration as the OD classification criteria. (a) Distribution of different levels of chromatic aberrations in AODLibpro Test. (b) Performance (PSNR) of FoundCAC under different chromatic aberration levels.

Then, because the configuration of the EAOD algorithm does not include settings for a cemented doublet structure, the optimization imposes no strong constraint on chromatic aberration, which causes many generated samples to exhibit noticeable chromatic aberration. Figure 10 shows the distribution of chromatic aberration severity in our AODLibpro Train, from which it can be seen that a considerable portion of the training samples reveal obvious chromatic aberration. We believe that these chromatically degraded samples in the training set endow the model with the ability to handle chromatic aberration, enabling it to effectively address purple fringing across the test cases.

E DETAILS FOR THE FOUNDCAC MODEL

E.1 DETAILS FOR PSF-VQVAE

The encoder and decoder of PSF-VQVAE each use 3 groups of ResBlocks, with corresponding downsampling or upsampling convolutions in every group. The latent space for representation and feature processing operates at 1/8 of the input resolution and has $n_z = 256$ channels. The structures of the encoder and decoder and the latent space feature dimensionality apply equally to ODN and FoundCAC, so we do not elaborate further. The codebook contains $K = 1024$ code vectors with a feature dimension of 512. During feature matching, two additional 1×1 convolution layers are applied before and after matching to handle feature dimension mismatches. These designs and settings follow [Chen et al. \(2022a\)](#); [Esser et al. \(2021\)](#).

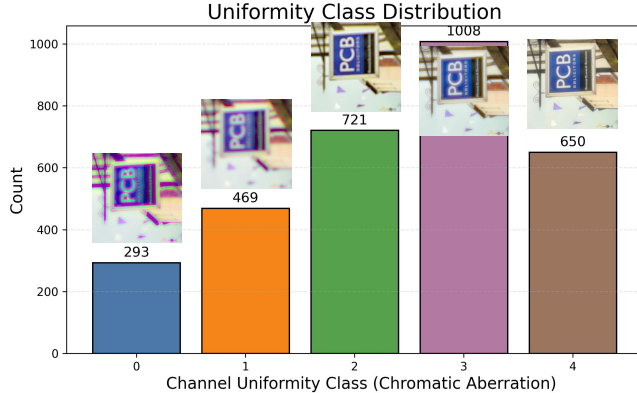


Figure 10: Distribution of different chromatic aberration levels in AODLibpro Train. Visualization cases for each level are also provided.

E.2 DETAILS FOR ODN

For the ODN fusion module F_{ODN} , we adopt Spatial Feature Transformation (SFT) followed by a cross attention module to generate the OD image from a clear input conditioned on PSF features that encode spatial variation patterns. This fusion form allows the two features to interact over the full spatial domain and enables PSF features to spatially modulate intermediate ODN features, achieving the OD modeling we need. We do not use a deep fusion backbone as in the CAC stage, because the OD process does not involve solving an ill-posed problem and therefore does not require many parameters or modules for deep fusion. In addition, since ODN acts as a constraint throughout training, excessive modules would increase the training cost. While richer ODN architectures and fusion variants may further strengthen the constraint, our goal here is to verify that the ODN constraint helps learn a useful PSF latent representation, so we leave broader design exploration to future work.

E.3 DETAILS FOR CAC STAGE

For FoundCAC (RRDB), we use 6 RRDB layers from [Wang et al. \(2018\)](#) as the deep fusion backbone. For FoundCAC (Swin), we adopt 4 RSTB layers in [Liang et al. \(2021\)](#). For the RRDB layer, *num_grow_chn* is set to 128, corresponding to a feature channel dimension of 256. For the RSTB layer, we set *blk_depth*, *num_heads*, and *window_size* to 6, 8, and 8, respectively. Since our RSTB operates at 1/8 input resolution, FoundCAC achieves faster inference than SwinIR, which uses RSTB at 1/4 resolution. In F_{CAC} , we adopt concatenation as the first step because our goal is to demonstrate that LPR can effectively guide CAC, and concatenation followed by deep fusion is an intuitive approach. Exploring more efficient fusion strategies is also an interesting direction for future work.

F DETAILED SETTINGS FOR MAIN EXPERIMENTS

F.1 DETAILS ON IMAGING SIMULATION

For AODLibpro Train, AODLibpro Test, and *RealLens-Sim*, we obtain the paired OD images corresponding to each lens design via imaging simulation. The imaging simulator from DeepLens ([Yang et al., 2024](#)) is adopted, considering its precise calculation of PSFs and simulation of OD images by patch-wise convolution. Specifically, we feed the design files of each sample in these LensLibs (in Zemax or parameter table format) into DeepLens for ray tracing to compute PSFs at 64 fields of view and 31 sampled wavelengths in the visible band. We match the closest sensor from the sensor library ($4\mu\text{m} - 2K$, $8\mu\text{m} - 2K$, $12\mu\text{m} - 2K$, $16\mu\text{m} - 2K$) based on the image height, discretize and sample the PSFs according to the pixel size, and stack them across RGB channels according to the wavelength response characteristics, ultimately obtaining the PSF arrays for each FoV and channel used in the simulation. It is worth noting that we applied equiva-

lent downsampling to sensor resolution and pixel size to facilitate the use of large-scale public 2K high-quality image datasets. Meanwhile, unifying the resolution also helps to systematically control variables to build a benchmark for exploring the CAC task. Finally, the computed PSFs are used to convert clear images into the corresponding OD images via patch-wise convolution, while the pipeline also accounts for sensor ISP and noise, as in most imaging simulation workflows (Chen et al., 2021a;b). For each lens in the 3 datasets, we will open source its Zemax design file, the computed PSF array, and the simulated paired OD images.

F.2 MOTIVATION FOR SETTING AODLIBPRO TEST

Previous studies on blind aberration correction have applied specific test data (Eboli et al., 2022; Gong et al., 2024; Jiang et al., 2024b), which makes it inconvenient to evaluate the performance of model paradigms. In this situation, the OD distributions of test lenses vary widely and unpredictably across works, so evaluations often measure the joint effect of training data and the model paradigm rather than the paradigm’s own ability to learn OD from data. Therefore, with training fixed on AODLibpro Train, we propose constructing AODLibpro Test as a benchmark for evaluating CAC networks. This benchmark has the following advantages: i) lenses in Train and Test are non-overlapping samples drawn from the same EAOD-generated lens source, which ensures that OD distributions in Test are independently unseen while keeping the domain gap moderate, thereby focusing on the paradigm’s ability to learn ODs; ii) constructing Test also uses the hybrid sampling basis, yielding OD distributions that are uniform across spatial variation patterns and severity, with no data bias, thus enabling reliable evaluation of comprehensive CAC performance. We believe this benchmark setup can promote exploration of model paradigms and help ensure that the validations of various model designs are effective. All results in Table 3,4,7 are obtained under this training and testing setup.

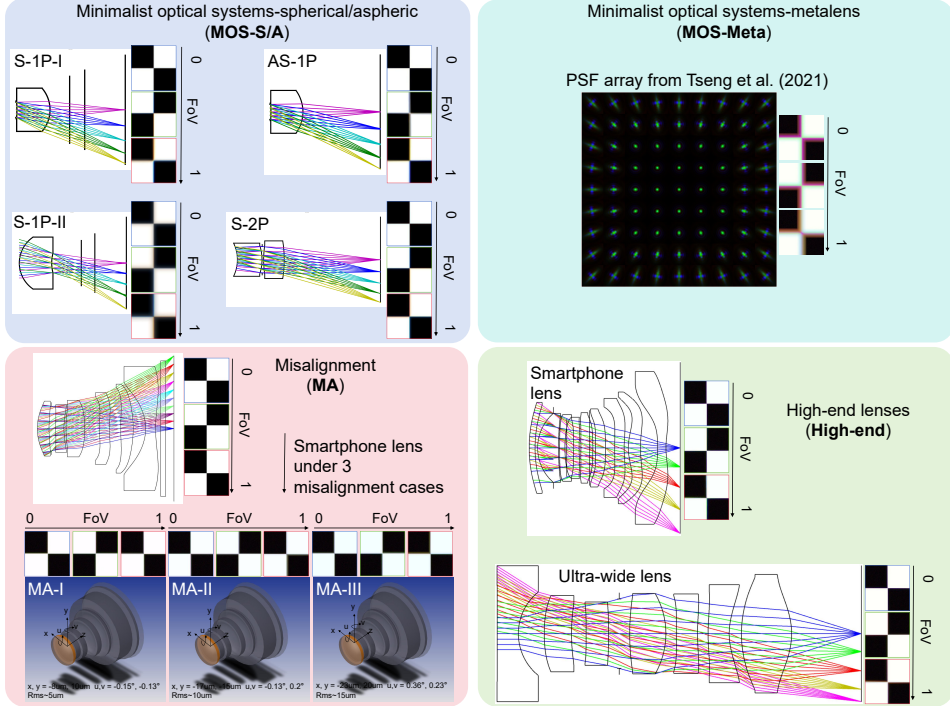


Figure 11: Illustration of lens designs, settings, and OD patterns for *RealLens-Sim*.

F.3 ILLUSTRATION OF LENS DESIGNS IN *RealLens-Sim*

Figure 11 shows the structures of the test lenses used in *RealLens-Sim* and example imaging results. The lenses are sourced from open source designs in the literature or from designs manually created by optical designers based on specifications in public patents or the needs of minimalist applications.

In addition, we consider lens misalignment, a common but rarely addressed real-world factor that induces OD. This typically occurs when the PSF size under the nominal lens design is below one pixel, that is, no OD, but the decentering and tilt errors in manufacturing and assembly lead to random unknown OD in the final imaging results. We select a smartphone lens whose original design yields no sensor sampled OD, set 3 groups of random decentering and tilt errors with increasing magnitude within its tolerance range, and then perform ray tracing to compute PSFs for imaging simulation.

Unlike AODLibpro Test, which provides a comprehensive evaluation in terms of OD severity and spatial variation patterns in the imaging results, *RealLens-Sim* aims to provide test data from the perspective of lens types across real-world application scenarios, reflecting the practicality of the overall blind aberration correction framework and assessing the combined performance of training data and model paradigm. Admittedly, lens design cases in the real world are innumerable, and many are not open source, so one cannot include them all in the tests. Nevertheless, the lens types, application scenarios, and OD distribution types covered by *RealLens-Sim* are the broadest among known open source data, allowing it to serve as a strong evaluation benchmark for assessing the generalization of blind aberration correction methods. In addition, because these lenses are manually designed by optical designers, they are out of domain relative to the LensLib generated by AOD methods, which can provide a fairer evaluation setting.

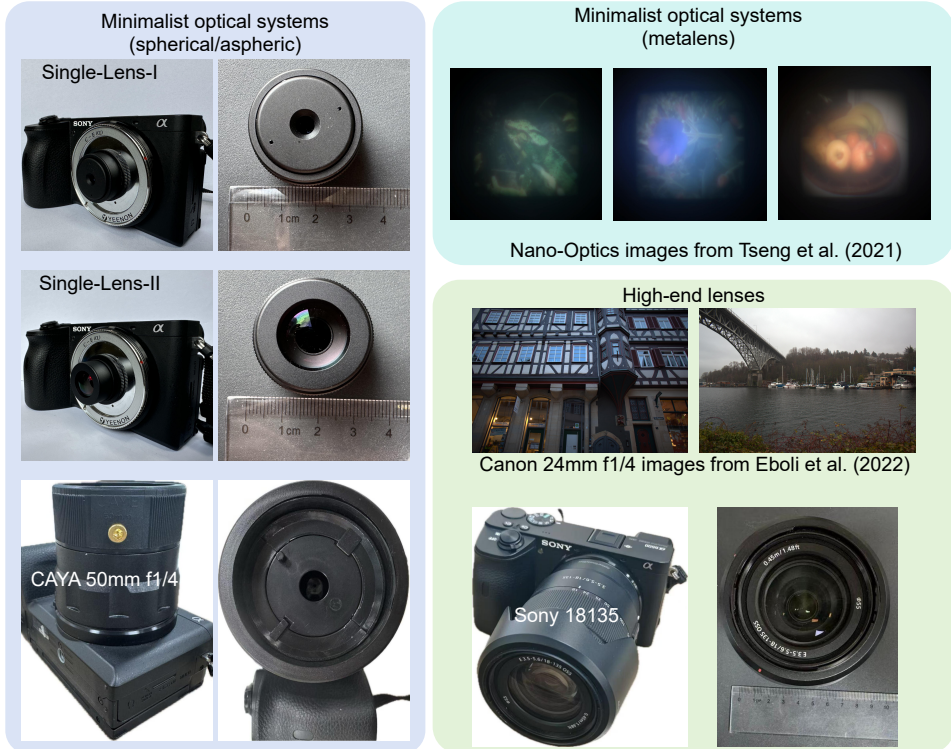


Figure 12: Schematic of the real snap setups for each lens in *RealLens-Snap*. For all devices whose setups are shown, we use images snapped in real-world scenes, while for the others we directly use their open-source images (Tseng et al., 2021; Eboli et al., 2022).

F.4 ILLUSTRATION OF CAPTURE DETAILS FOR *RealLens-Snap*

We show the imaging setups used for our real-world captures in *RealLens-Snap* in Figure 12. In addition, the nano-optics data come from 3 open-source images in Tseng et al. (2021), and the Canon 4mm f1/4 data come from two open-source images in Eboli et al. (2022). Quantitative evaluation on *RealLens-Snap* directly reflects the potential of blind aberration correction to improve image quality on real-world terminals. Given the difficulty of collecting real-world lenses under various applications for shooting, we strive to construct *RealLens-Snap* covering commonly used

scenarios for blind aberration correction, such as minimalist optical systems, high-end photographic equipment, and metalens imaging. The selected systems exhibit distinct OD distributions, enabling a more comprehensive evaluation of the representative methods. To the best of our knowledge, we are the first work of blind aberration correction whose evaluation simultaneously covers minimalist optical systems with severe aberrations and high-end lenses with mild aberrations. We also hope to continuously collect more real snapped images with OD in future work to broaden application scenarios.

F.5 DETAILS FOR COMPETING BLIND ABERRATION CORRECTION METHODS

For the fast two-step method (Eboli et al., 2022), since we are dealing with spatially varying OD, we process the OD images using 256×256 tiles with 128 overlap, and keep all other settings the same as the defaults in its open-source code. Regarding the choice of an open-source, pretrained universal IR model for comparison, we consider it a primary option for users without an optical background to handle unknown OD, because such methods aim to use highly generalizable large models to address real-world unknown degradations. We directly load its pretrained weights (Zhang et al., 2024) to process our OD data. For all LensLib-PT methods (Gong et al., 2024; Jiang et al., 2024c; Côté et al., 2021; Jiang et al., 2024b) on the data side, we generate paired OD images using the same pipeline as AODLibpro based on each LensLib’s PSF arrays. Considering the inconsistency in the number of lenses across different Lenslibs, to ensure a fair comparison, we keep the total number of training images identical by changing the number of GT images degraded per lens. For the method in Gong et al. (2024), although the proposed model paradigm is insightful, we use only its LensLib ZEBASELib to train SwinIR for comparison rather than the proposed model because it is not open-sourced. For the pipelines in Jiang et al. (2024c) and Côté et al. (2021), since they provide only the ideas for constructing a LensLib and do not involve CAC model design, we likewise use only the LensLibs built following their ideas and use SwinIR as the model. For the SwinIR used as the network, we adopt the same \mathcal{L}_{CAC} as FoundCAC (L1 loss and perceptual loss), with a batch size of 16 and 200K training iterations.

F.6 DETAILS FOR TRAINING COMPETING CAC NETWORKS

For all CAC networks compared in Table 3, we use their architectures and retrain them on AODLibpro Train. To fully exploit the capability of each method, we adopt the official training configurations. Moreover, to ensure fairness in perceptual metrics, all methods are additionally trained with perceptual loss.

F.7 DETAILS FOR TABLE 4, 7, AND 8.

Figure 13 together with Figure 6, show the model paradigms of the compared PSF representation methods in Table 4. For a fair comparison, the network architectures of the modules, the losses used in the VQVAE, and the CAC and ODN losses involved in these paradigms are all kept consistent with those in the final LPR. We also omit the illustration of PSF-VQVAE+ODN&CAC, because this pipeline only adds a CAC network for supervision on top of LPR pre-training and applies that CAC network as initialization in the CAC stage. Meanwhile, the baseline models in Table 7 and 8 are the first model paradigm shown in Figure 6.

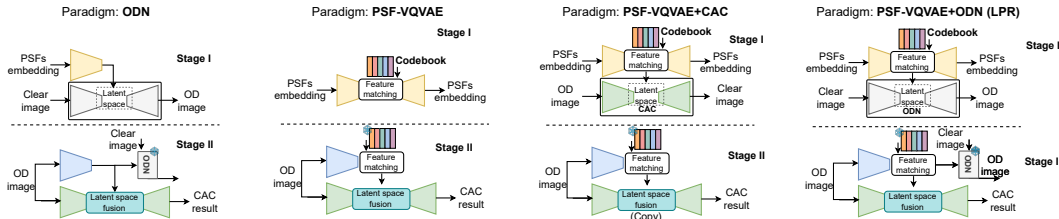


Figure 13: Illustration of the model paradigms in Table 4. Some of the paradigms have been shown in Figure 6, which are omitted here (baseline, GT-PSFs-guided, PSFs prediction, and PSFs feature prediction).

G MORE EXPERIMENTAL RESULTS

G.1 ADDITIONAL RESULTS FOR THE EVALUATION ON EACH LENS OF *RealLens-Sim*

Table 10 reports per-lens results for each method as a complement to Table 2. Figure 14, 15, 16, and 17 shows qualitative CAC results of representative methods on selected *RealLens-Sim* lenses. On lenses in MOS with more severe aberrations, when other methods still show residual OD, OmniLens++ produces relatively clearer results without introducing false details and is close to the GT. For milder aberrations such as MA and high-end lenses, OmniLens++ can further correct aberrations to improve image quality while avoiding over-sharpening, yielding more natural results. These additional results highlight the good generalization of OmniLens++.

Table 10: Per-lens results for competing blind lens aberration correction methods on *RealLens-Sim*.

Method	S-1P-I			S-1P-II			AS-1P			S-2P			Nano-Optics		
	PSNR	SSIM	LPIPS	PSNR	SSIM	LPIPS	PSNR	SSIM	LPIPS	PSNR	SSIM	LPIPS	PSNR	SSIM	LPIPS
Fast two-step	20.48	0.747	0.2783	18.87	0.681	0.4133	22.50	0.696	0.3077	20.90	0.758	0.2514	21.58	0.655	0.4488
Universal IR	20.05	0.761	0.2670	18.92	0.726	0.2698	22.00	0.734	0.2742	20.39	0.765	0.2351	21.36	0.687	0.4229
ZEBASELib-PT	23.84	0.813	0.2695	21.59	0.752	0.3736	22.26	0.767	0.3077	24.67	0.831	0.2369	18.14	0.679	0.4931
ZernikeLib-PT	26.39	0.855	0.1548	23.01	0.791	0.2534	23.61	0.779	0.1840	24.62	0.865	0.1442	20.50	0.707	0.3806
AODLib-LensNet-PT	23.70	0.826	0.2572	21.30	0.751	0.3978	22.48	0.768	0.3002	24.91	0.841	0.2194	18.56	0.678	0.4993
AODLib-EAOD-PT	27.83	0.880	0.1354	25.77	0.832	0.2002	24.29	0.803	0.1828	29.00	0.898	0.1202	20.10	0.740	0.3805
AODLibpro-PT (SwinIR)	27.30	0.877	0.1442	25.73	0.835	0.1923	26.79	0.837	0.1558	28.69	0.894	0.1242	22.02	0.754	0.3391
AODLibpro-PT (FoundCAC)	27.54	0.880	0.1396	25.63	0.840	0.1773	27.24	0.841	0.1466	27.96	0.896	0.1226	23.32	0.769	0.3145
Method	MA-I			MA-II			MA-III			Ultra-wide lens			Smartphone lens		
	PSNR	SSIM	LPIPS	PSNR	SSIM	LPIPS	PSNR	SSIM	LPIPS	PSNR	SSIM	LPIPS	PSNR	SSIM	LPIPS
Fast two-step	28.05	0.789	0.1708	26.54	0.742	0.1796	26.81	0.771	0.1930	28.23	0.828	0.1710	27.97	0.825	0.1725
Universal IR	27.96	0.822	0.1699	27.40	0.805	0.1776	25.34	0.770	0.1864	29.33	0.851	0.1464	30.06	0.864	0.1383
ZEBASELib-PT	26.66	0.855	0.1071	26.53	0.846	0.1232	24.55	0.809	0.1518	27.80	0.898	0.1123	28.52	0.905	0.0982
ZernikeLib-PT	26.47	0.881	0.1130	25.02	0.833	0.1173	24.01	0.835	0.1440	26.58	0.897	0.0929	27.87	0.900	0.0934
AODLib-LensNet-PT	27.12	0.886	0.1024	25.90	0.840	0.1185	24.87	0.847	0.1464	27.33	0.901	0.1041	27.66	0.908	0.0912
AODLib-EAOD-PT	26.80	0.892	0.0939	26.41	0.855	0.0932	24.86	0.836	0.1174	27.64	0.901	0.0968	27.80	0.906	0.0938
AODLibpro-PT (SwinIR)	27.44	0.895	0.0968	26.48	0.858	0.0951	25.51	0.840	0.1186	27.47	0.902	0.1005	27.41	0.906	0.0979
AODLibpro-PT (FoundCAC)	28.58	0.896	0.0917	27.50	0.864	0.0927	26.24	0.838	0.1101	28.76	0.902	0.0981	28.86	0.906	0.0968

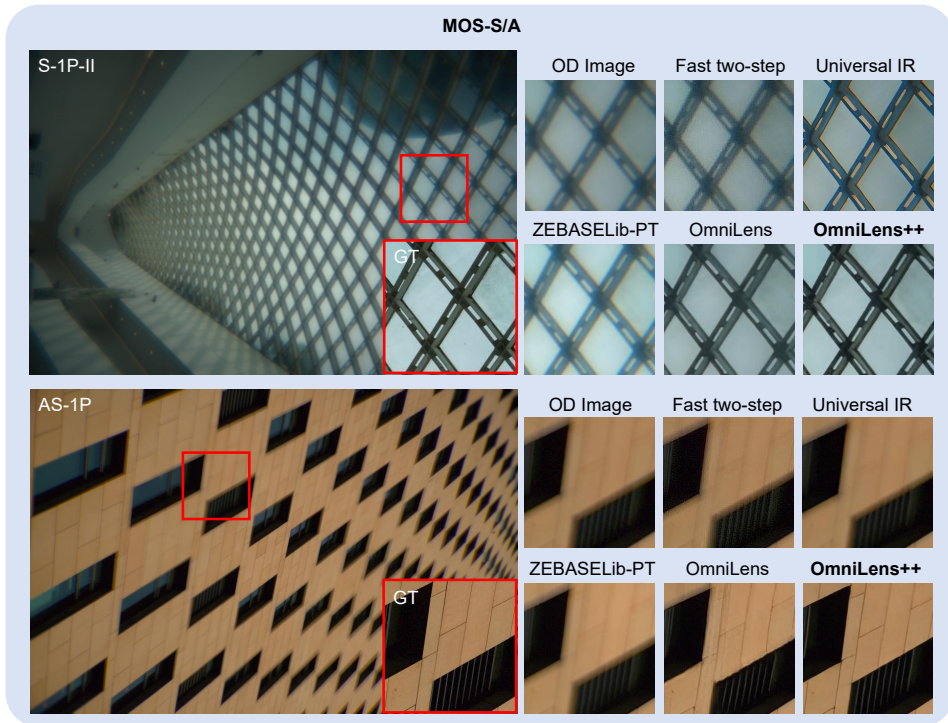


Figure 14: Visual comparison on MOS-S/A. S-1P-II and AS-1P are selected as the representative spherical and aspheric lenses for their distinct OD patterns.

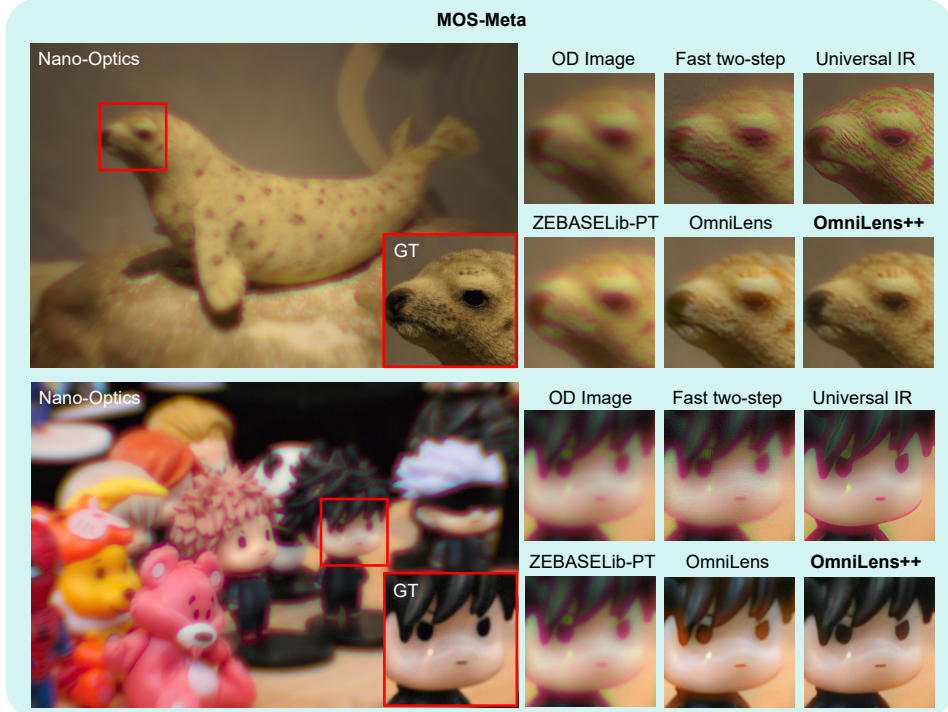


Figure 15: Visual comparison on MOS-Meta.

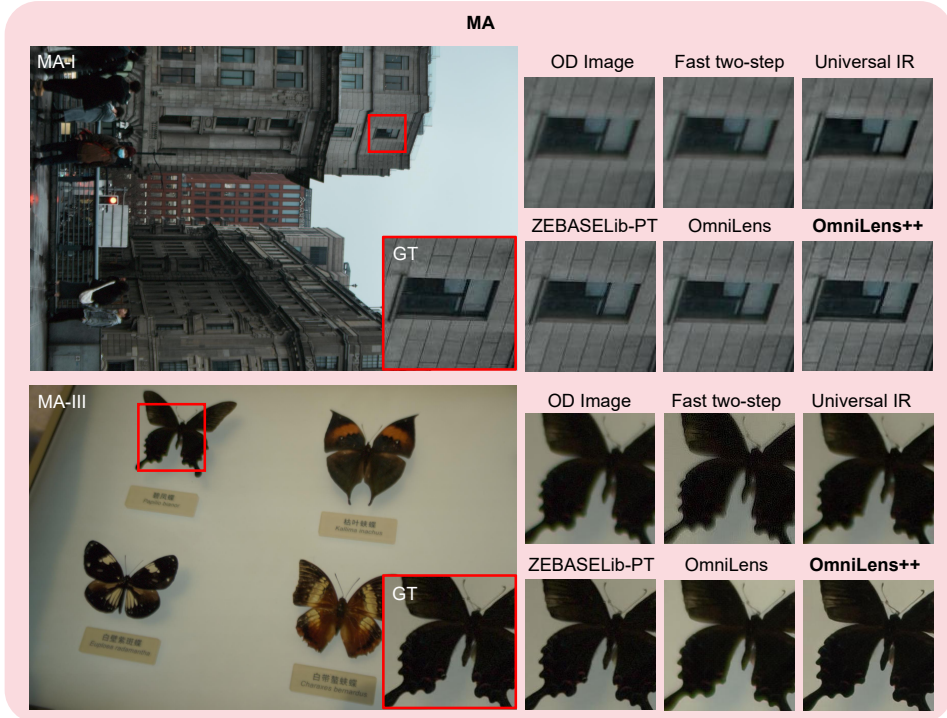


Figure 16: Visual comparison on MA. We present results under the minimum misalignment (MA-I) and maximum alignment (MA-III) settings.

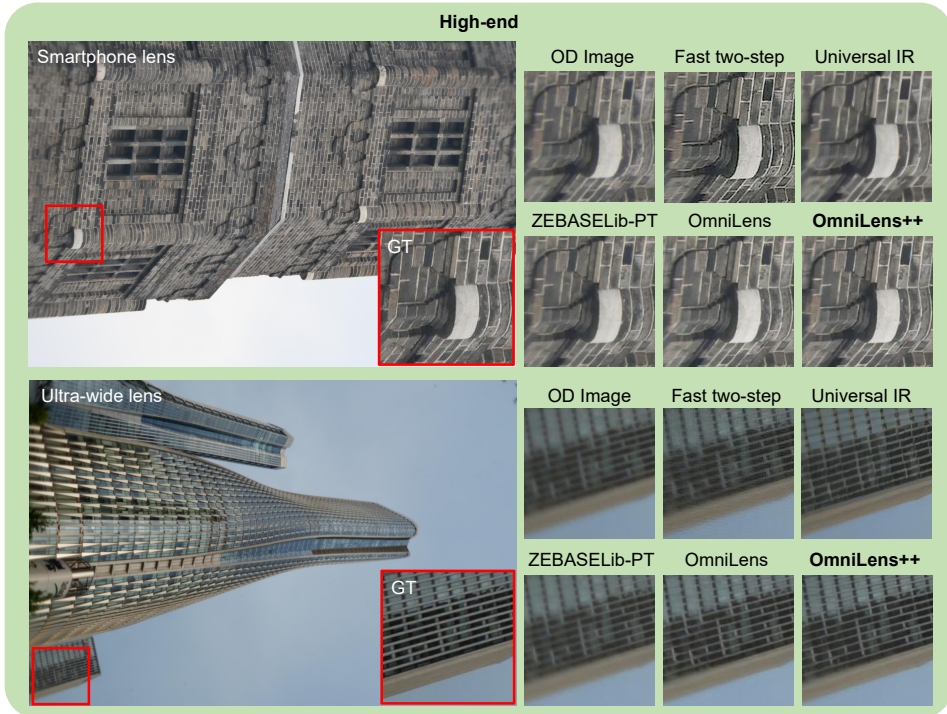


Figure 17: Visual comparison on High-end.

G.2 ADDITIONAL ANALYSIS FOR SUPPLEMENTED SPECIFICATIONS.

As shown in Figure 18, using OD-Class, we visualize the OD distributions of lens-source samples generated by EAOD under the baseline specifications, with aspheric surface added, and with both aspheric surface (A.S.) and image plane perturbation (I.P.P.) added. The results are consistent with our motivation for introducing these factors, namely that both specifications lead the optimized lenses to exhibit new OD patterns. Specifically, adding A.S. yields more samples with severe OD because the increased number of optimization parameters makes optimization more difficult, while adding image-plane perturbations yields more OD-Class “2” and “3” samples because shifting the image plane position changes the in-focus field.

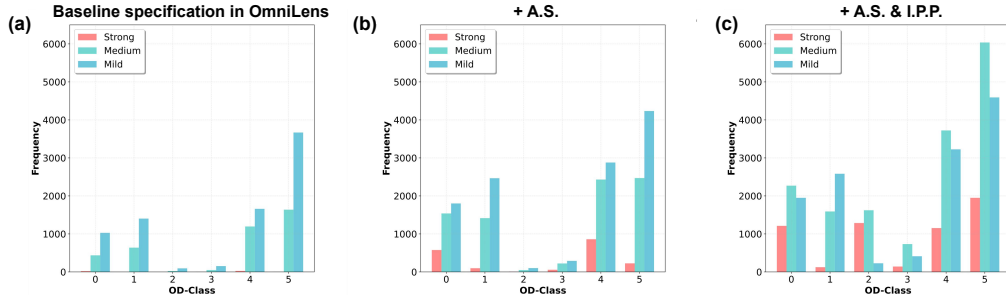


Figure 18: OD distributions of the lens source generated under different specification settings.

G.3 ADDITIONAL ABLATIONS ON CODEBOOK SIZE

We sweep the codebook size K to test whether allocating more entries for key latent PSF features benefits LPR. Table 11 shows no meaningful gains for FoundCAC from larger K . For the current PSF diversity in AODLibpro, $K = 1024$ appears sufficient to capture latent optical priors, whereas larger K likely accumulates ineffective codes, complicates matching, and yields less reliable PSF guidance. A promising direction is to devise training strategies for larger codebooks that learn more effective degradation representations.

Table 11: Ablations on codebook size in LPR

K	PSNR	LPIPS
512	28.53	0.1301
2048	28.78	0.1297
1024	28.67	0.1277

G.4 VISUALIZATION OF THE LEARNED PSF REPRESENTATION

To understand why LPR provides better guidance for CAC than the PSF representations compared in Table 4, we visualize in Figure 19 the predicted PSF features under each representation before feature fusion. For two OD patterns with completely different distributions, one spatially non-uniform with moderate overall severity and one more spatially uniform with strong overall severity, LPR shows clear differences between the predicted PSF features and can partially reflect their intuitive OD patterns. Specifically, for S-1P-I, the attention regions of the PSF features predicted by LPR are mostly located at the peripheral FoVs, whereas for S-1P-II, the attention regions are almost global. These match the OD patterns exhibited in the OD image, indicating that LPR effectively learns OD priors, which other representations cannot achieve. In PSF-VQVAE, the attention distribution is very sparse and lacks clear regularity; while in ODN, the PSF features contain more scene details, and the attention is almost the same across different OD patterns, indicating that it fails to decouple the OD priors encoded by PSFs. These pieces of evidence further demonstrate the superiority of LPR in combining the two. In addition, even when directly supervising the prediction with GT

PSF features, the predicted PSF features can hardly intuitively reflect the OD pattern, although the differences across OD cases are better than ODN.

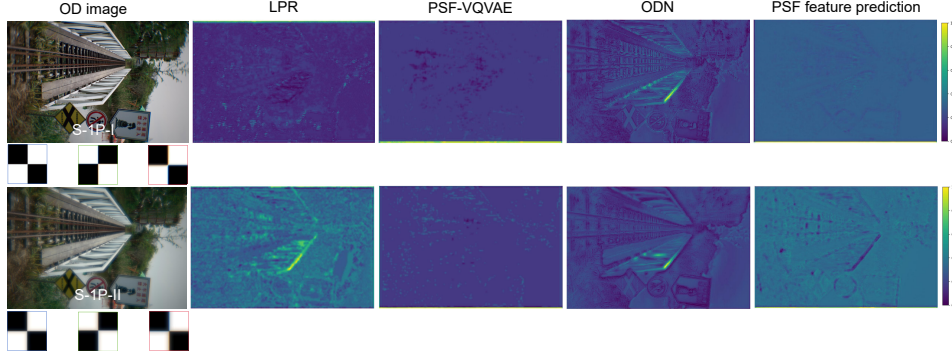


Figure 19: Visualization of the predicted latent PSF features. We use the PSF feature map before fusion to visualize the guidance of different PSF representations. The input OD image and an example of its OD distribution are shown in the first row.

G.5 NUMERICAL EVALUATION ON *RealLens-Snap*

To more fairly and comprehensively evaluate the performance of representative blind aberration correction pipelines on real-snapped data *RealLens-Snap*, we conduct quantitative evaluation using common non-reference image quality metrics CLIPQA (Wang et al., 2023), NIQE (Mittal et al., 2013), and MANIQA (Yang et al., 2022), with results shown in Table 12. Consistent with the results in Figure 4, even though these metrics exhibit some instability, the proposed OmniLens++ still performs better overall, highlighting its stronger generalization.

Table 12: Per-lens numerical evaluation for competing blind lens aberration correction methods on *RealLens-Snap*.

Method	Single-Lens-I			Single-Lens-II			CAYA 50mm f1/4		
	CLIPQA↑	NIQE↓	MANIQA↑	CLIPQA↑	NIQE↓	MANIQA↑	CLIPQA↑	NIQE↓	MANIQA↑
Fast two-step	0.341	3.903	0.218	0.341	4.907	0.227	0.324	3.835	0.180
Universal IR	0.470	3.548	0.310	0.407	5.575	0.282	0.411	3.843	0.266
ZEBASELlib-PT	0.336	5.493	0.211	0.319	7.265	0.213	0.299	5.966	0.202
OmniLens	0.383	4.789	0.289	0.392	5.718	0.327	0.376	4.311	0.277
OmniLens++	0.398	4.061	0.272	0.456	4.792	0.310	0.393	3.929	0.273
Method	Nano-Optics			Canon 24mm f1/4			Sony 18135		
	CLIPQA↑	NIQE↓	MANIQA↑	CLIPQA↑	NIQE↓	MANIQA↑	CLIPQA↑	NIQE↓	MANIQA↑
Fast two-step	0.342	7.013	0.231	0.469	3.292	0.343	0.560	2.826	0.303
Universal IR	0.389	8.172	0.263	0.433	3.388	0.332	0.489	3.050	0.317
ZEBASELlib-PT	0.360	9.522	0.299	0.519	4.182	0.359	0.512	4.264	0.322
OmniLens	0.332	8.735	0.285	0.492	3.971	0.369	0.499	3.955	0.328
OmniLens++	0.370	8.126	0.266	0.538	3.790	0.339	0.500	3.395	0.315

G.6 ADDITIONAL VISUAL RESULTS ON *RealLens-Snap*

To further demonstrate the effectiveness of our method, we present additional comparison results between the proposed OmniLens++ and competing approaches on real-world images captured with different lenses. Results on simple spherical and aspherical lenses are shown in Figures 20, 21, and 22, those on metalens are shown in Figure 23, and those on high-end lenses are shown in Figures 24 and 25. The proposed OmniLens++ consistently produces favorable CAC results on various lens types, further demonstrating its zero-shot capability in handling diverse aberrations. Specifically, for MOS, OmniLens++ mitigates severe aberrations and delivers promising CAC results where competing methods perform unsatisfactorily. For high-end DSLR lenses, it further alleviates residual aberrations, including chromatic aberration, while avoiding over-sharpening.

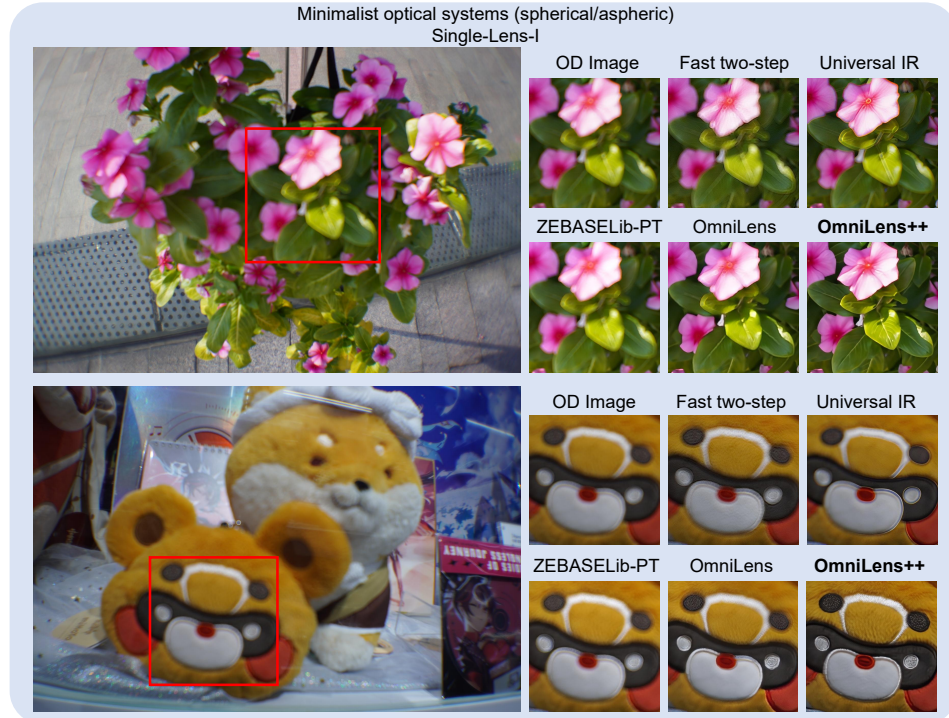


Figure 20: Visual comparison on Single-Lens-I.

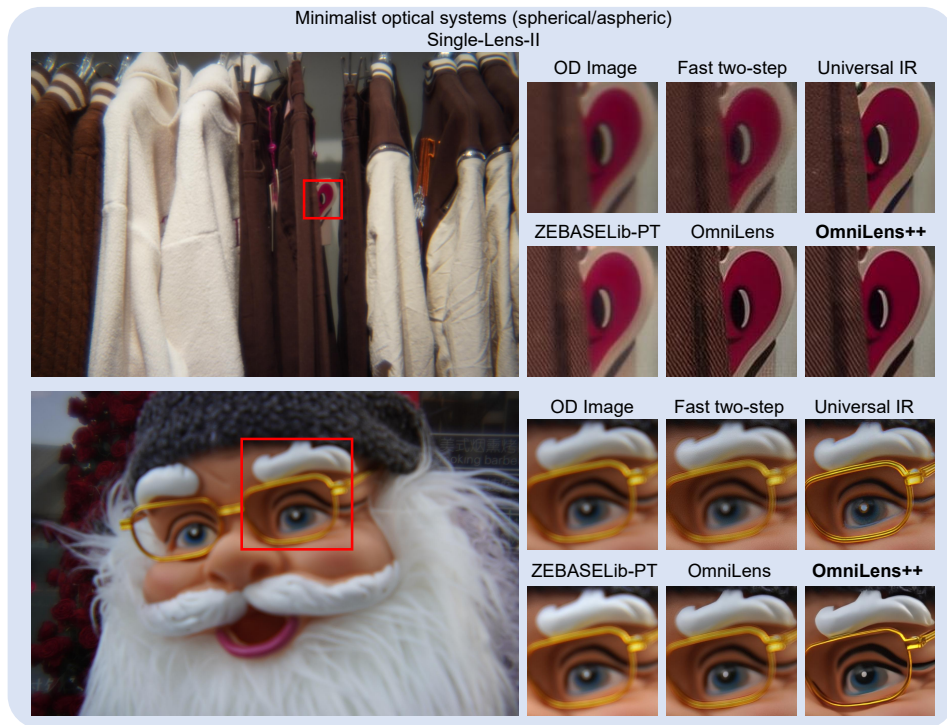


Figure 21: Visual comparison on Single-Lens-II.

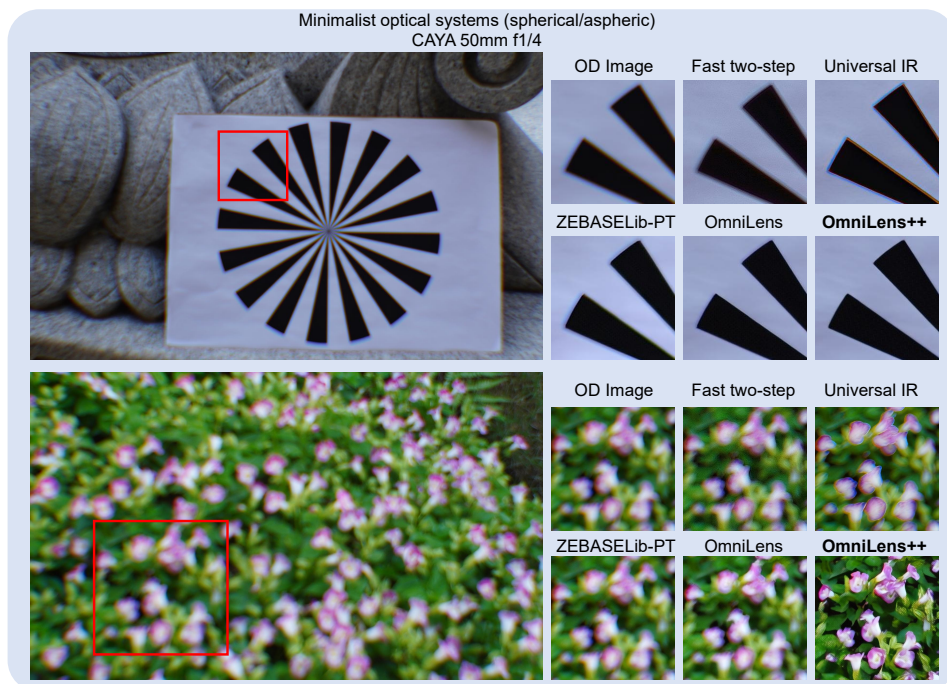


Figure 22: Visual comparison on CAYA 50mm f1/4.

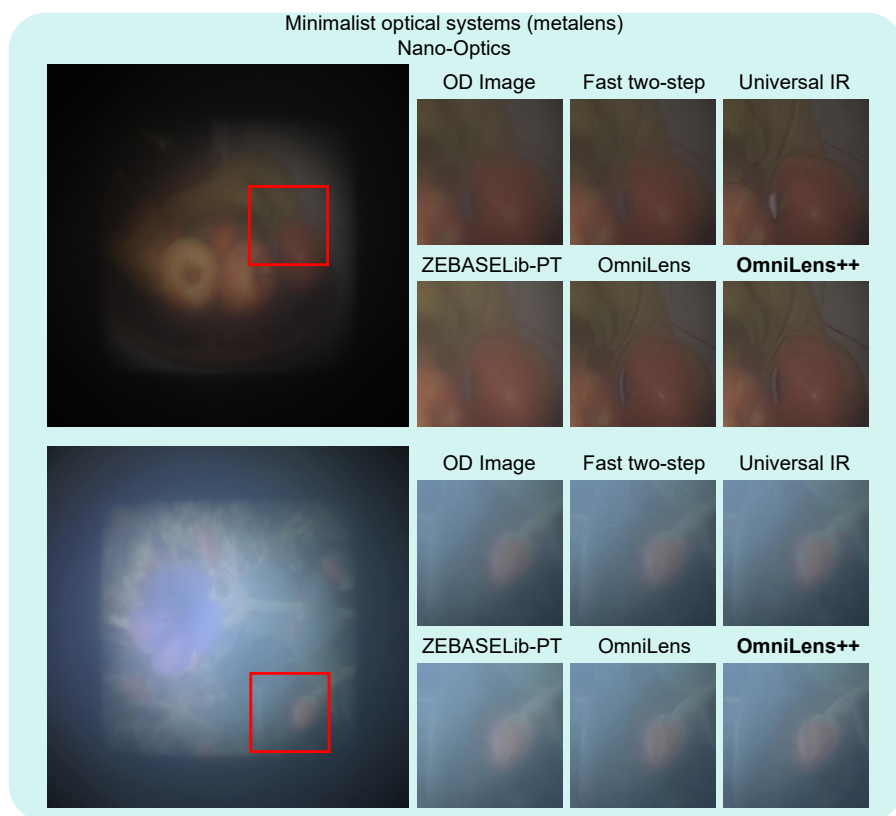
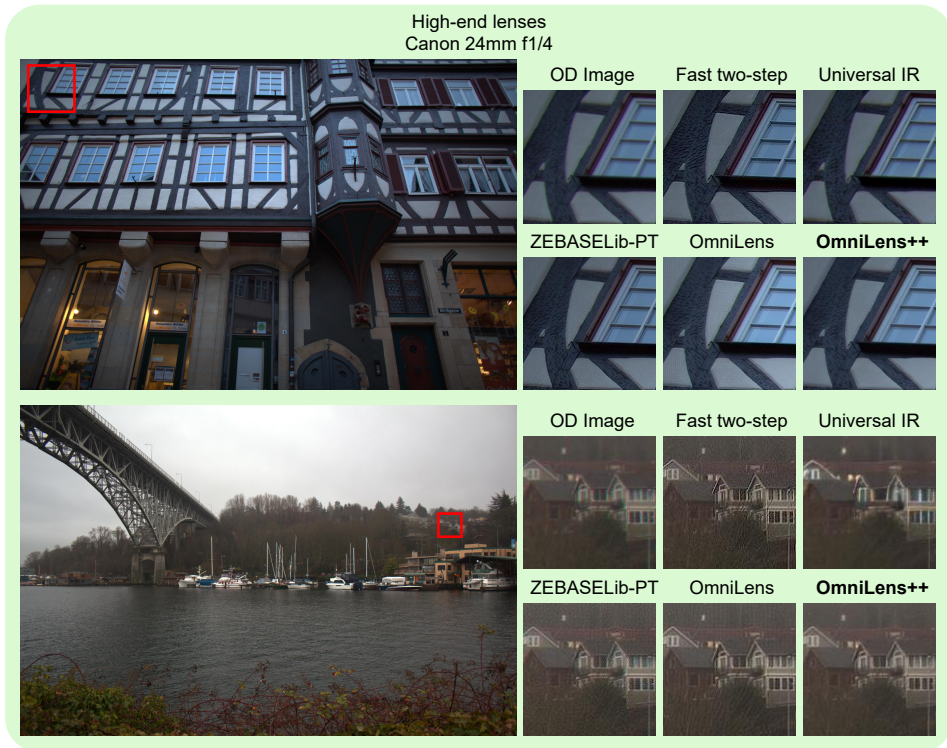
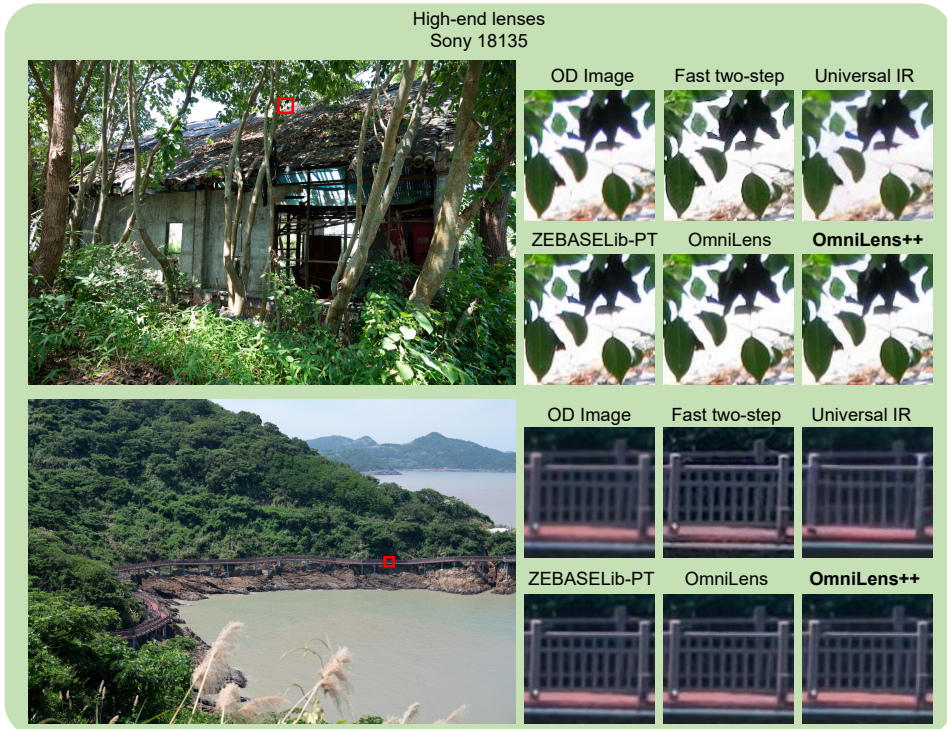


Figure 23: Visual comparison on Nano-Optics.

Figure 24: Visual comparison on *Canon 24mm f1/4*.Figure 25: Visual comparison on *Sony 18135*.